Flexible and scalable control of T cell memory by a reversible epigenetic switch

Kathleen Abadie[1*], Elisa C. Clark[1*], Obinna Ukogu[2], Wei Yang[3], Riza M. Daza[3], Kenneth K.H. Ng[1], Jumana Fathima[1], Allan L. Wang[1], Avinash Bhandoola[4], Armita Nourmohammad[2,5,6], Jay Shendure[3,7,8,9,11#], Junyue Cao[3,9,10,#], Hao Yuan Kueh[1,11,#]

[1]Department of Bioengineering, University of Washington, Seattle, WA, USA

[2]Department of Applied Mathematics, University of Washington, Seattle, WA, US

[3]Department of Genome Sciences, University of Washington, Seattle, WA, USA

[4]T-Cell Biology and Development Unit, Laboratory of Genome Integrity, Center for Cancer Research, National Cancer Institute, National Institute of Health, Bethesda, MD, USA

[5]Department of Physics, University of Washington, Seattle, WA, USA

[6] Fred Hutchinson Cancer Research Center, Seattle, USA

[7]Brotman Baty Institute for Precision Medicine, Seattle, WA, USA

[8]Allen Discovery Center for Cell Lineage Tracing, Seattle, WA, USA

[9]Howard Hughes Medical Institute, Seattle, WA, USA

[10]Laboratory of Single-cell Genomics and Population Dynamics, The Rockefeller University, New York, NY, USA

[11]Institute for Stem Cell and Regenerative Medicine, University of Washington, Seattle, WA, USA

[*,#]These authors contributed equally to this manuscript

25

26

Abstract

The immune system encodes information about the severity of a pathogenic threat in the quantity and type of memory cell populations formed in response. This encoding emerges from the decisions of lymphocytes to maintain or lose self-renewal and memory potential during a challenge. By tracking CD8 T cells at the single-cell and clonal level using time-resolved transcriptomics and quantitative imaging, we identify a flexible memory strategy, whereby T cells initially choose whether to maintain or lose memory potential early after antigen recognition, but following pathogen clearance may regain memory potential if initially lost. This flexibility is implemented by a cis-epigenetic switch silencing the memory regulator TCF1 in a stochastic, reversible manner in response to stimulatory inputs. Mathematical modeling shows how this strategy allows memory cell numbers to scale robustly with pathogen virulence and immune response magnitudes. Thus, flexibility in cellular decision making ensures optimal immune responses against diverse threats.

43 **Main**

44 The immune system keeps a memory of prior infections with information about the inducing
45 threat. This memory is encoded by the numbers and types of memory lymphocytes generated
46 upon challenge. The quantity of memory T cells, in particular, scales with the magnitude of a
47 prior infection, such that the memory population is a fixed fraction of the T cell number at the
48 infection peak, across a range of pathogenic challenges[1–3]. This scaling in memory production is
49 robust across T cell clones with different epitope specificities and allows the body to generate
50 memory proportional to the severity of the pathogenic challenge. The regulatory mechanisms
51 that enable this critical feature of adaptive immunity are not well understood.

52

53 The size and characteristics of the memory compartment are determined by the fate decision-
54 making strategies of T cells responding to an acute infection[4]. As naive CD8 T cells respond to
55 antigens, they must decide whether and when to maintain long-term viability and self-renewal
56 potential, and thereby persist to form memory cells as the infection is cleared. One class of
57 models posits that cells make this decision early after antigen encounter, and in a mutually
58 exclusive manner with effector differentiation (Fig. 1A)[5–7]. Under this model, memory cells form
59 directly from naive cells without first passing through an effector phase, but through an early
60 lineage bifurcation that concurrently gives rise to short-lived effector cells. A second class of
61 models posits that cells decide later, only after they have undergone effector differentiation (Fig.
62 1A)[8–10]. In this strategy, cytotoxic effectors that maintain memory potential populate the memory
63 compartment upon infection clearance. However, in contrast with both models, it is also possible
64 that this process is inherently flexible[11], such that T cells have multiple opportunities to commit
65 to the memory state. From a social and cognitive sciences perspective[12,13], flexibility in decision

making allows individuals to adapt and better respond to uncertain and dynamic environments; in the immune system, such flexibility may allow T cells to optimize memory formation for threats whose properties might only manifest as they unfold in time. It is unclear whether there exists such flexibility in T cell memory formation and, if so, what its underlying mechanisms and functional roles are.

In this study, we sought to elucidate the memory decision-making dynamics of CD8 T cells by following the regulation of TCF1 (encoded by *Tcf7*), a transcription factor essential for memory cell generation[14]. *Tcf7* is expressed in naive and memory cells, where it is crucial for maintaining self-renewal, and is silenced during effector differentiation, resulting in loss of memory potential and entry into a short-lived state[5,15]. To follow *Tcf7* regulation and memory decision-making in a controlled environment where cells can be continuously observed and signaling inputs carefully manipulated, we developed an *ex vivo* system to mimic stimulation of T cells by acute challenge. Using this system and complementary testing *in vivo*, we uncover a flexible decision-making strategy: T cells can gain or lose memory potential at multiple junctures after antigen encounter, and do so in a stochastic and reversible manner. Mathematical modeling reveals that this flexible decision-making strategy allows for the number of memory cells to scale linearly with total numbers of expanded T cells at the peak of infection, thereby encoding information about the severity of the prior threat.

A minimal *ex vivo* system for effector and memory differentiation

In our system, naive ($CD44^{-}CD62L^{+}$) CD8 T cells with a knock-in YFP reporter for *Tcf7*[16] are activated with plate-immobilized anti-CD3 and anti-CD28 antibodies and IL-2, together with

89 additional cytokines present during acute infection (IL-12, IL-7, and IL-15[17–19]). These
90 conditions minimize variability in the exposure of individual cells to stimulatory signals,
91 enabling cell-intrinsic lineage control mechanisms to be studied apart from environmental
92 heterogeneity.
93
94 In this system, all cells begin dividing rapidly after 24 hours and upregulate the transmembrane
95 glycoprotein CD44, indicating uniform activation (Fig. 1B). Activated cells downregulate *Tcf7*
96 and the lymph node-homing adhesion molecule CD62L, consistent with effector differentiation.
97 The inflammatory cytokines IL-12 and IFN-β1 enhance *Tcf7*-YFP silencing (Fig. 1C, Fig. S1C-
98 D), consistent with their roles in driving effector differentiation[20,21]. When TCR stimulation
99 (anti-CD3/CD28) and inflammation (IL-12) are removed to mimic pathogen clearance, the cells
100 demonstrate a population-level increase in CD62L and *Tcf7*-YFP while continuing to divide, as
101 previously observed[4]. *Tcf7* and CD62L levels are heterogeneous both during stimulation and
102 after removal, suggestive of an early memory and effector differentiation decision. YFP levels
103 closely matched TCF1 protein levels throughout activation, validating use of the reporter in this
104 system (Fig. S1A-B).
105
106 **Naive cells bifurcate early into effectors and memory precursors**
107 To determine whether the heterogeneity in *Tcf7* and CD62L downregulation reflects early
108 memory and effector programming (Fig. 1), we analyzed *ex vivo* activated cells using the
109 temporally-resolved single-cell transcriptome sequencing method, *sci-fate*[22]. Here, metabolic
110 labeling of newly-synthesized transcripts reveals a cell's current activity state apart from its
111 history[22,23] (Fig. 2A). We subjected cells at days 1, 2, and 4 to 4-thiouridine (4sU) pulse-labeling

112 for 2 hrs, followed by sequencing and analysis as previously described[22]. We obtained old and
113 new transcriptomes for ~17,000 single cells, with a median of 17,574 total and 2,529 new
114 transcripts detected per cell (Fig. S2A). To disentangle effector and memory gene programs from
115 other activation-induced programs, we performed an integrative analysis of our temporally-
116 resolved transcriptome data and existing transcription factor (TF) binding data[24] to identify TF
117 modules, consisting of co-regulated groups of TFs and their cognate target genes (see Methods).
118 This analysis revealed two main TF modules, a cell cycle module and a T cell differentiation
119 module, the latter further separable into submodules that included known regulators of effector
120 and memory differentiation (Fig. 2B; Fig. S2C).
121
122 By visualizing cell states using genes in the T cell differentiation module for Uniform Manifold
123 Approximation and Projection (UMAP) dimensionality reduction, we resolved distinct effector
124 and memory states with coherence between timepoints (Fig. 2C; Fig. S2B, D). Unsupervised
125 clustering and differential gene expression analysis revealed distinct early and late (A vs. B)
126 effector (E1 and E2) and memory precursor (MP) states. E1 and E2 cells exhibited higher
127 expression of the effector-associated genes *Gzmb, Ifng, Tbx21, Zeb2,* and *IL12rb2,* while MP
128 cells had higher expression of the stem- and memory-associated factors *Bach2, Lef1, Tcf7, Sell*,
129 and *Slamf6*, and lower expression of effector-associated genes (Fig. 2D-E; Fig. S2E-F;
130 Supplementary Table 1-2)[25]. These differential gene expression patterns were present at day 2
131 and amplified at day 4.
132
133 Consistent with an early fate bifurcation, RNA velocity vectors calculated using reads from
134 newly synthesized transcripts originate from the undifferentiated state (U), and flow along

135 separate effector and memory branches[26] (Fig. 2F). To gain insight into the dynamics of genes
136 differentially regulated between divergent trajectories, we visualized their expression over
137 pseudotime along each trajectory (Fig. 2G; Supplementary Table 3). This analysis, together with
138 RNA velocity and TF activity analysis (Fig. 2H-I), identified effector and memory regulators
139 with greatest differential regulation along their respective trajectories. *Tbx21, Egr1,* and *Irf4*,
140 among other effector regulatory genes, were specifically active along the E1 trajectory, while a
141 distinct set of effector regulators, including *Eomes, Bhlhe40*, *Stat5a* and *Stat3*, characterize the
142 E2 trajectory. This effector heterogeneity and its potential influence on downstream
143 differentiation will be interesting to investigate in future studies but is not further pursued here.
144 Finally, regulators of T cell stemness and survival, including *Tcf7, Myb, Mxd4* and *Fli1*, were
145 active in the MP trajectory. *Tcf7* was the most significantly differentially expressed gene
146 between trajectories, upregulated early along the MP trajectory and absent in both E1 and E2
147 trajectories. Its expression furthermore coincided with that of target genes identified through TF
148 linkage that promote self-renewal, such as *Ikzf2*, *Sesn3*, *Aff3*, and *Pecam1* (CD31). Thus, *Tcf7* is
149 a critical driver of this early divergent memory trajectory in our system.
150

151 **The early effector and memory decision occurs heterogeneously within clones**

152 The divergence of cells into effector and memory lineages, occurring even under the strong,
153 uniform stimulatory conditions of our *ex vivo* system, is suggestive of a cell-intrinsic regulatory
154 mechanism involving *Tcf7* that generates heterogeneity in fate outcomes. To elucidate the degree
155 to which this decision is heterogeneous within cell lineages amid constant environmental signals,
156 we acquired multi-day time-lapse movies of clonal CD8 T cell lineages during activation with
157 continuous measurement of *Tcf7* reporter levels (Fig. 3). As T cells are difficult to track with live

158 imaging due to their high mobility, tendency to adhere to one another, and rapid proliferation, we
159 optimized adhesion conditions and computational analyses that allow continuous tracking of a
160 fate regulating TF across clonal CD8 T cell lineages (Fig. 3; Fig. S3; see Methods)[27]. Using this
161 method, we tracked a total of 120 clonal lineages over 4 days and an average of 4.4 cell
162 generations.
163
164 Naive cells in these time-lapse movies start small, adhere to the antibody-bound plate, acquire
165 CD69 expression, increase dramatically in size, and divide rapidly after 1-2 days (Fig. S3G;
166 Supplemental movie 1). Strikingly, individual activating T cell clones often gave rise to *Tcf7*
167 high and low subpopulations (Fig. 3A; Fig. S3J; Supplementary Movie 1), indicating that the
168 effector and memory decision is made heterogeneously within clones. Of note, *Tcf7* low and high
169 cells showed similar degrees of attachment to the surface, indicating that these intra-clonal
170 differences are not due to differences in TCR stimulation, but more likely due to cell-intrinsic
171 mechanisms generating heterogeneity in *Tcf7* silencing.
172
173 Differences in *Tcf7*-YFP levels after multiple cell divisions likely stem from earlier *Tcf7*
174 silencing events propagated through dilution of the stable fluorescent protein by cell division. To
175 pinpoint the timing of early regulatory events that give rise to these differences in *Tcf7*-YFP
176 levels, we calculated the *Tcf7* promoter activity over time in single cells, defined as the rate at
177 which total *Tcf7*-YFP levels increase over time, using a Hidden Markov Model (HMM) to assign
178 *Tcf7* promoter activity states to each cell at each timepoint and identify switching points between
179 those states (Fig. 3A-C; Fig. S3A-F; see Methods).
180

181 This analysis revealed that cells silence *Tcf7* expression at variable times after the onset of
182 stimulation, and can do so as early as the first cell division as well as at later generations. Cells
183 activated the *Tcf7* promoter prior to the first cell division, reflecting exit from quiescence, and
184 then proceeded to switch the *Tcf7* promoter to a silent state. The timing at which the *Tcf7*
185 promoter transitioned to the silent state varied between cell tracks both within and between cell
186 lineages, consistent with observed heterogeneity in *Tcf7*-YFP levels within clones (Fig. 3A-D).
187 Removing IL-12 increased the fraction of cells in an active promoter state (Fig. 3C,E). Silent
188 *Tcf7* promoter states persisted across multiple cell divisions (Fig. 3A; Fig. S3I-J) and thus
189 represent heritable regulatory changes as opposed to more transient dynamics such as
190 transcriptional bursting. These results provide evidence that a cell-intrinsic *Tcf7* silencing event,
191 occurring heterogeneously within clones, underlies the early divergence in effector and memory
192 states.
193
194 **A stochastic epigenetic switch controlling *Tcf7* silencing underlies the early effector and**
195 **memory decision**
196 Heterogeneity in *Tcf7* silencing could derive from asymmetric cell division[6,28], whereby cell fate
197 determinants partition unequally, giving rise to discordant behavior between two sister cells.
198 Alternatively, this heterogeneity could result from stochastic control[29–31], whereby two sisters
199 would make *Tcf7* silencing decisions independently. While two sister cells could still make
200 different decisions, they would silence *Tcf7* discordantly no more frequently than expected by
201 chance. To test these predictions, we analyzed the fractions of daughter cell pairs that silence
202 *Tcf7* either discordantly (ON/OFF) or concordantly (OFF/OFF), doing so for cell pairs across all
203 cell generations, with or without IL-12 (Fig. 3F). By plotting concordant (OFF/OFF) versus

204 discordant (ON/OFF) sister pair fractions, we found that all data points adhered to a theoretical
205 curve representing the expected relationship between sister pair fractions for independent
206 regulation (Fig. 3G). Consistently, by statistical analysis using a modified Cohen's kappa
207 coefficient (κ'), we found that daughter cells were no more likely to make discordant decisions
208 than expected by chance (Fig. 3H; Supplementary Table 4). These findings support the view that
209 *Tcf7* silences in a stochastic manner to drive divergent decision making within clones.
210
211 Epigenetic switching mechanisms, involving changes in chromatin modifications or
212 conformation at gene loci, can introduce stochastic rate-limiting steps to gene activation or
213 silencing[32–34]. As *Tcf7* silencing involves repressive DNA or histone methylation[14,20,35,36], it
214 could be gated by such a mechanism. Epigenetic mechanisms act in *cis* at individual gene loci
215 and therefore would silence each *Tcf7* locus independently. To test for this mechanism, we
216 compared *Tcf7*-YFP silencing kinetics in cells from mice homozygous and heterozygous for the
217 reporter, with the prediction that homozygous reporter cells would yield a smaller population of
218 YFP-low cells, since both loci need to silence for loss of reporter expression (Fig. 3I-J, Fig.
219 S3K). Indeed, the *Tcf7*-YFP silent population was significantly smaller in homozygous reporter
220 cells and increased with IL-12, consistent with a *cis*-epigenetic silencing mechanism modulated
221 by inflammation. Together, these results provide evidence that a stochastic *cis*-epigenetic switch,
222 tunable by external stimuli, controls the early decision of naive cells to silence *Tcf7* expression
223 and memory potential.
224
225 **Reversibility of *Tcf7* silencing enables a late memory decision**

226 *Tcf7* silencing has been proposed to be an irreversible event that marks a 'point of no return' for
227 effector differentiation and loss of memory potential[5,37]. Conversely, various studies have
228 demonstrated that cells that acquire cytotoxic effector function are able to populate memory
229 compartments after an infection is resolved[8,9,38], suggesting that *Tcf7*-silenced effectors may still
230 be able to reactivate *Tcf7* and reacquire memory potential. Our data thus far provide evidence for
231 an early T cell decision to abandon or maintain memory potential, driven by stochasticity in
232 antigen-driven *Tcf7* silencing, but do not exclude the possibility that effector cells can reverse
233 their decisions and regain memory potential later after withdrawal of stimulation.
234
235 To test this possibility, we sorted *Tcf7*-YFP low and *Tcf7*-YFP high cells after initial culture and
236 subjected them to reculture with variable stimulation conditions *ex vivo* (Fig. 4A). As expected,
237 sorted *Tcf7*-YFP high cells maintained *Tcf7*-YFP expression without stimulation but underwent
238 heterogeneous silencing under continuing stimulation (Fig. 4B-C, Fig. S4A-B). Furthermore,
239 *Tcf7*-YFP low cells maintained a silent state upon continued stimulation, as observed. Strikingly,
240 however, upon stimulation withdrawal, *Tcf7* reactivated, with the fraction of *Tcf7* expressing
241 cells increasing over 6 days. *Tcf7* reactivation upon stimulation withdrawal coincided with CD25
242 downregulation and CD62L upregulation, suggesting re-entry into a memory state (Fig 4D). To
243 test whether *Tcf7* reactivation and reacquisition of memory potential also occurs *in vivo*, we
244 transferred *Tcf7*-YFP low and high cells into naive recipient mice (Fig. 4A), and assayed their
245 *Tcf7* expression at successive time points. Indeed, *Tcf7*-YFP low cells reactivated *Tcf7*
246 expression progressively in the spleen and lymph nodes over 10 days with concomitant increases
247 in CD62L and IL7Rα, indicating reacquisition of a memory phenotype (Fig. 4E-G; Fig. S4C-D).
248

249 We next used clonal live imaging of sorted *Tcf7*-YFP low cells confined in microwells to test if
250 *Tcf7* reactivation is heterogeneous within individual effector clones, as would be expected if
251 reactivation occurs via reversal of stochastic *cis*-epigenetic silencing (Fig. 3). Consistent with
252 reactivation observed from bulk starting populations, individual *Tcf7* silenced cells gave rise to
253 *Tcf7* high cells (Fig 4H-I; Supplementary Movies 2 and 3; Supplementary Table 5). Similar to
254 the initial *Tcf7* silencing event, reactivation was heterogeneous within clones. Reactivation
255 occurred only after multiple divisions, which may reflect the need for cell division for permissive
256 chromatin state changes. Overall, these results indicate that cells that have silenced *Tcf7* and
257 relinquished memory potential can reverse this decision later, after resolution of an immune
258 challenge.
259
260 ***Tcf7* high cells formed through early and late decisions acquire a common memory**
261 **program**
262 Our results show that memory cells can arise through two pathways: a "naive to memory" (NM)
263 pathway, whereby some cells maintain *Tcf7* expression during initial antigen stimulation, and a
264 "naive to effector to memory" (NEM) pathway, by which cells that have silenced *Tcf7* and
265 entered an effector state can turn expression back on after stimulation removal. To determine
266 whether *Tcf7* high cells emerging through these two pathways both have genomic and functional
267 memory programs, we subjected them to transcriptomic, epigenomic, and cytokine secretion
268 analysis, alongside control *in vivo* naive ($CD44^{-}CD62L^{+}$), memory ($CD44^{+}CD62L^{+}$), and *ex vivo*
269 generated effector cells (Fig. 5).
270

271 Remarkably, NM and NEM cells showed similar memory characteristics, despite different *Tcf7*
272 regulatory history. They were both more similar to naive and memory *in vivo* controls compared
273 to *ex vivo* generated effector cells in their shared expression of memory-defining genes, though
274 they also maintained some effector characteristics, in line with their recent stimulation (Fig. 5A-
275 C; Fig. S5A). Similar to memory controls, NM and NEM cells demonstrated greater TNF-α and
276 IFN-γ secretion upon re-stimulation compared to naive cells (Fig. 5D-E). NM and NEM cells
277 were most similar in global chromatin accessibility to memory controls (Fig. 5F; Fig. S5B-C).
278 NEM cells recovered similar *Tcf7* accessibility to NM cells (Fig. 5G). At the *Ifng* locus,
279 intermediate accessibility of NM and NEM cells between naive and effector controls suggests
280 that both were poised for rapid recall response, and accessibility at other memory- and effector-
281 associated loci support this conclusion (Fig. S5D).
282
283 While NM and NEM cells were largely similar, notable differences in tissue localization and
284 gene expression suggest they may be primed for different functional memory properties *in vivo*.
285 Transferred *Tcf7* high cells showed greater engraftment in secondary lymphoid organs than *Tcf7*
286 low sorted cells, suggesting different homing capabilities (Fig. S5E). NEM cells also had higher
287 expression and accessibility of some effector-associated genes compared to NM, possibly
288 indicative of enhanced effector capabilities or an effector memory state[37,38] (Fig. S5F-G).
289 Overall, both NM and NEM decision strategies give rise to cells with genomic and functional
290 characteristics of memory, suggesting that memory formation may proceed through a flexible
291 decision-making strategy, allowing both for memory and effector divergence during the initial
292 immune challenge and for effector reacquisition of memory potential after the challenge is
293 resolved.

294

295 **Multiple paths to memory enable robust encoding of pathogen experience through memory**

296 **population size**

297 Flexibility in memory decision-making may have functional benefits, and may in particular

298 allow for scaling of memory population sizes with immune response magnitudes. To test this

299 idea, we used mathematical modeling to evaluate different T cell decision-making strategies in

300 their memory outcomes in response to pathogens of different virulence, modeled as having

301 different rates of replication (see Mathematical Appendix). In our first model, we consider the

302 flexible strategy we observed (Fig. 6A). Here, naive T cells (T_n) initially transition to a Tcf7-

303 expressing memory-competent state (MC, T_m) that divides upon exposure to pathogen (v), but

304 stops dividing and persists upon pathogen clearance. These cells can either maintain memory

305 competence upon continuing stimulation, or transition to *Tcf7*-silent effector state (T_e), where

306 they control pathogen growth, but are short-lived. Based on our findings (Fig. 3), this transition

307 to an effector state is stochastic, with a probabilistic rate that increases with pathogen. Effector

308 cells can reverse *Tcf7* silencing and re-enter the memory-competent state in the absence of

309 pathogen, as we observe (Fig. 4).

310

311 Mathematical simulations of this flexible decision model recapitulate the canonical features of

312 the T cell response to acute infection (Fig. 6B; Fig. S6A-B). T cells expand rapidly in response to

313 pathogen, reaching a peak 4-8 days after infection onset that consists mostly of effector cells,

314 followed by a contraction to a stable, lower level of memory-competent cells (T_m). Consistent

315 with known studies[1,39], the quantity of memory cells is ~5% of the peak cell number.

316

317 In response to pathogens with varying replication rates, this flexible decision model allows
318 memory cells to form robustly and scale linearly with peak cell expansion numbers. Increasing
319 effector expansion with faster pathogen replication was accompanied by a proportional increase
320 in memory cells, such that the memory fraction relative to the peak T cell number remained
321 constant (Fig. 6B and 6C – top, yellow shading, γ_v>0.02/hr). This relation is given by:

322 $$f_{T_m} = \frac{\beta_{e,m}}{\beta_{e,m}+\delta_e}$$

323 where $\beta_{e,m}$ is the maximum effector to memory conversion rate and δ_e is the effector death rate.
324 This scaling breaks down when pathogen replication is slow (γ_v<0.02/hr): reduced antigen
325 encounter decreases the probability of the early effector cell decision, such that the number of
326 memory cells generated converges to the starting naive cell number rather than increasing with
327 pathogen replication rate. This ensures a baseline level of memory amid weak challenges that do
328 not elicit a full effector response[3].
329
330 To ask whether flexibility is necessary for scalable memory encoding, we analyzed two
331 alternative decision models, where memory decisions are made at only one juncture. The early
332 decision model, where naive cells irreversibly commit to the *Tcf7*-silent effector state, generated
333 robust memory upon challenge with slow-dividing pathogens but cannot reproduce the linear
334 scaling of the memory population to the peak population in response to faster-replicating
335 pathogens (Fig. 6C, middle; Fig. S6C-F; see also Mathematical Appendix). Conversely, the late
336 decision model, where naive cells transition obligatorily to the effector state and decide later
337 whether to regain memory competence, generated constant memory fractions upon stronger
338 challenges but attenuated memory populations in response to weaker challenges (Fig. 6C,

339 bottom; Fig. S6G-H). These analyses underscore the importance of flexibility in memory
340 decision making for optimal long-term immunity against variable threats.
341
342 **Discussion**
343 Our finding that reversible epigenetic silencing of *Tcf7* generates inherent flexibility in the T cell
344 memory decision reconciles two prevailing models for memory development that have often
345 been regarded as mutually opposed. While there is evidence that memory cells can form both
346 directly from naive cells with little or no effector differentiation and from effector cells that
347 dedifferentiate upon infection clearance[8,9], no model has explained how both pathways can
348 coexist. In this mechanism, stochastic control of *Tcf7* silencing enables early divergent memory
349 and effector decision making, and its reversibility enables late effector dedifferentiation. Antigen
350 and inflammatory signals tune the decision-making probabilities at both junctures (Fig. 2-4) and
351 would thereby influence which pathway would predominate across challenges that differ in
352 signal duration and intensity[40]. This study, together with others[33], implicate stochastic epigenetic
353 switches as drivers of cellular diversification in the immune system. Through regulatory events
354 that initiate over timescales spanning cell generations, these switches allow multiple cell
355 populations to emerge in defined numbers without strict spatially-organized cues[41], facilitating
356 division of labor for optimal pathogen defense.
357
358 Our modeling results lay the groundwork for understanding how the adaptive immune system
359 can encode information about the nature and severity of a pathogen in its memory cell population
360 (Fig. 6). In future work, it will be interesting to determine whether other pathogen features, such
361 as antigenicity or latency, may also be encoded quantitatively. Our findings that memory cells

362 emerging from different decision points may differ in their functional properties (Fig. S5E-G)
363 raise the possibility that flexible decision making could underlie qualitative encoding of
364 pathogen information through the generation of heterogeneous memory subsets[37,38]. In future
365 work, it will be interesting to investigate the extent to which each decision pathway is utilized
366 under various threats *in vivo* and whether cells emerging from different pathways are
367 functionally heterogeneous[42].
368
369 Overall, our study highlights the utility of plasticity in cell fate decision making in biological
370 systems. From a strategic standpoint, flexibility enables decision makers to change their minds
371 with new information, allowing them to mount optimal responses amid uncertain
372 circumstances[12]. For immune cells responding to a pathogen, an ability to reassess prior
373 decisions, as opposed to making early commitments, may enable bet-hedging and greater
374 responsiveness as an immune challenge evolves. Observed plasticity in mammalian stem cell
375 fate decision making[43,44] may similarly allow the body to rapidly adapt its regenerative output to
376 changing physiological needs[45]. A fuller consideration of flexibility in cellular decision making,
377 along with its mechanisms and roles, will shed light into design principles of these systems and
378 provide valuable insight for harnessing cells as environmentally-responsive therapeutic agents.

Acknowledgments

We thank members of the Kueh, Nourmohammad, and Shendure labs, as well as Philip Greenberg, Jinfang Zhu, and Douglas Fowler for stimulating discussions and feedback, and William Noble for advice on statistical analysis methods. We also thank Sam Nguyen for help with brightfield image cell segmentation. This study was funded by an NIH/NIBIB Trailblazer Award (R21EB027327, to H.Y.K.) an NIH/NHGRI R01 grant (R01HG010632-01, to J.S.), NSF Graduate Research Fellowships (K.A., E.C.C.) , NSF CAREER award (grant No: 2045054, to A.N.), and startup funds from the Bioengineering Department at the University of Washington (H.Y.K.), the Department of Physics at the University of Washington (A.N.), and the Rockefeller University (J.C.). J.S. is an investigator of the Howard Hughes Medical Institute.

Author Contributions

K.A. and H.Y.K. conceived the study and designed the experiments. E.C.C., J.S. and J.C. contributed to experimental design. K.A. and E.C.C. performed the experiments and analyzed the data. J.C. performed the scRNA-seq experiments, and R.D. performed bulk RNAseq and ATACseq. W.Y. performed initial analysis on the scRNA-seq experiments. J.F. and A.L.W performed analysis on imaging data. K.K.H.N. helped set up the *ex vivo* T cell activation system. H.Y.K. developed the mathematical models and O.U., A.N., and H.Y.K. analyzed the

401 mathematical models. A.B. provided the *Tcf7*-YFP reporter mice and guidance. K.A. and H.Y.K
402 wrote the manuscript. E.C.C. contributed to the writing of the manuscript.
403
404 **Declaration of interests**
405 The authors declare no competing interests.
406
407 **Data availability**
408 The time-resolved single-cell RNA-seq and bulk RNA-seq and ATAC-seq data generated for this
409 study will be deposited in the Gene Expression Omnibus. All other data will be made available
410 upon reasonable request.
411
412 **Code availability**
413 Scripts for processing sequencing and imaging data are written in Python, R, and Matlab and will
414 be made available upon request at https://github.com/KuehLabUW.
415
416 **Figures**

Figure 1

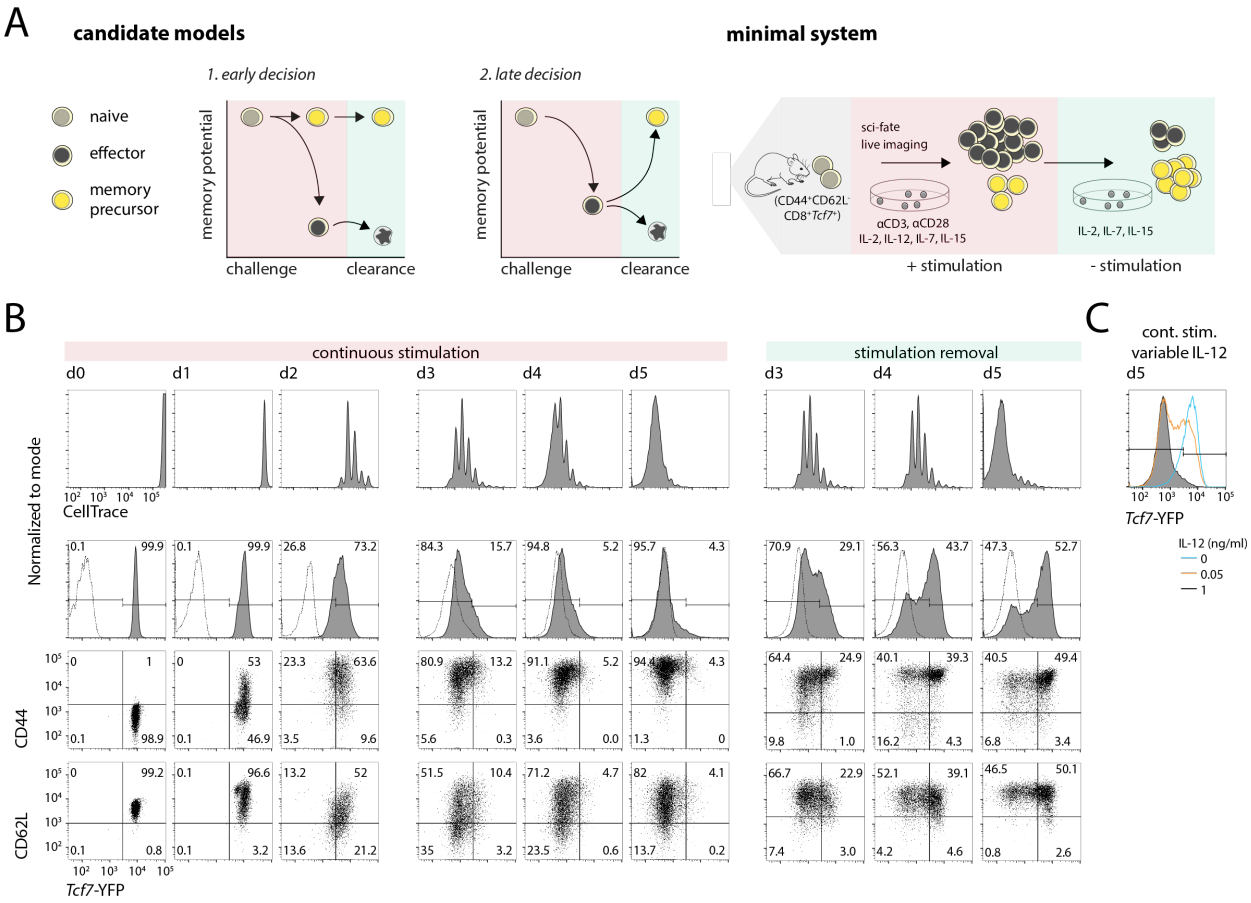

Figure 1: A minimal *ex vivo* system to track CD8 T cell effector and memory decision making dynamics. (**A**) Candidate decision-making strategies for CD8 T cell memory generation (left); a minimal *ex vivo* system for tracking memory decision-making dynamics at the single-cell level. (**B-C**) Naive CD8 T cells were isolated from *Tcf7*-YFP reporter mice, then cultured using this minimal *ex vivo* system. Flow cytometry plots show analysis of cultured CD8 T cells during initial stimulation for 2 days (left) and continued stimulation to day 5 (middle), or after stimulation withdrawal (removal of αCD3/αCD28 after day 2 and IL-12 after day 3) (right). (**C**) *Tcf7*-YFP silencing is tunable by IL-12 levels. Data are from a single experiment representative of at least 3 independent experiments.

Figure 2

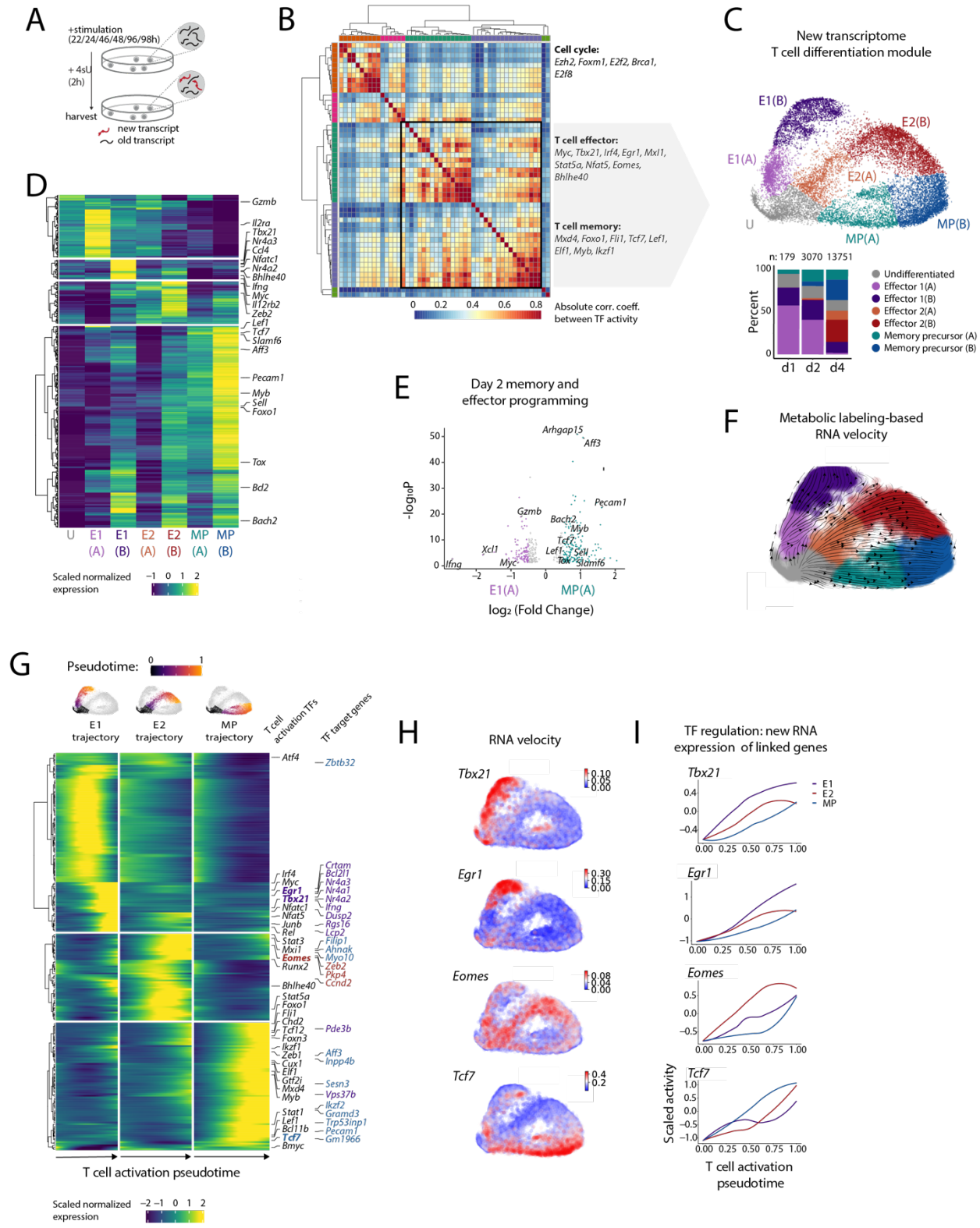
A
+stimulation
(22/24/46/48/96/98h)
+ 4sU
(2h)
harvest
new transcript
old transcript
B
Cell cycle:
Ezh2, Foxm1, E2f2, Brca1, E2f8
T cell effector:
Myc, Tbx21, Irf4, Egr1, Mxl1, Stat5a, Nfat5, Eomes, Bhlhe40
T cell memory:
Mxd4, Foxo1, Fli1, Tcf7, Lef1, Elf1, Myb, Ikzf1
Absolute corr. coeff. between TF activity
C
New transcriptome
T cell differentiation module
E1(B)
E2(B)
E1(A)
E2(A)
U
MP(A)
MP(B)
n: 179 3070 13751
Percent
d1 d2 d4
Undifferentiated
Effector 1(A)
Effector 1(B)
Effector 2(A)
Effector 2(B)
Memory precursor (A)
Memory precursor (B)
D
Gzmb
Il2ra
Tbx21
Nr4a3
Ccl4
Nfatc1
Nr4a2
Bhlhe40
Ifng
Myc
Il12rb2
Zeb2
Lef1
Tcf7
Slamf6
Aff3
Pecam1
Myb
Sell
Foxo1
Tox
Bcl2
Bach2
U E1 (A) E1 (B) E2 (A) E2 (B) MP (A) MP (B)
Scaled normalized expression
E
Day 2 memory and effector programming
-log10P
Arhgap15
Aff3
Pecam1
Gzmb
Bach2
Myb
Tcf7
Lef1
Sell
Tox
Slamf6
Xcl1
Ifng
Myc
E1(A)
MP(A)
log2 (Fold Change)
F
Metabolic labeling-based RNA velocity
G
Pseudotime:
E1 trajectory
E2 trajectory
MP trajectory
T cell activation TFs
TF target genes
Atf4
Zbtb32
Irf4
Myc
Egr1
Tbx21
Nfatc1
Nfat5
Junb
Rel
Stat3
Mxi1
Eomes
Runx2
Crtam
Bcl2l1
Nr4a3
Nr4a1
Nr4a2
Ifng
Dusp2
Rgs16
Lcp2
Fil1p1
Ahnak
Myo10
Zeb2
Pkp4
Ccnd2
Bhlhe40
Stat5a
Foxo1
Fli1
Chd2
Tcf12
Foxn3
Ikzf1
Zeb1
Cux1
Elf1
Gtf2i
Mxd4
Myb
Pde3b
Aff3
Inpp4b
Sesn3
Vps37b
Ikzf2
Gramd3
Trp53inp1
Pecam1
Gm1966
Stat1
Lef1
Bcl11b
Tcf7
Bmyc
T cell activation pseudotime
Scaled normalized expression
H
RNA velocity
Tbx21
Egr1
Eomes
Tcf7
I
TF regulation: new RNA expression of linked genes
Tbx21
Egr1
Eomes
Tcf7
E1
E2
MP
Scaled activity
T cell activation pseudotime

428

429 **Figure 2: Naive cells diverge into effector and memory states early after activation.** (**A**)
430 Naive CD8 T cells were activated as in Fig. 1A, with 0.05 ng/ml IL-12. After 1, 2, and 4 days,
431 cells were treated with 4sU for 2 hours to label new transcripts, then harvested for time-resolved
432 transcriptomics using *sci-fate*. (**B**) Heatmap showing the absolute Pearson's correlation
433 coefficient between the activities of pairs of TFs, generated using *sci-fate*. Key TFs in each
434 module are labeled at right. T cell differentiation module used for subsequent analysis is boxed.
435 (**C**) UMAP visualization of cells based on the activity of T cell differentiation-related TF
436 module, using newly synthesized mRNA, colored by cluster ID (top). Percentage of cells in each
437 T cell activation state cluster after indicated days (bottom). (**D**) Aggregated expression (scaled,
438 $\log_{10}$ normalized) of top 400 differentially expressed (DE) genes between clusters ($q < 3 \times 10^{-45}$
439 for all genes except for *Ifng*, $q = 7.3 \times 10^{-29}$). (**E**) DE genes between E1(A) and MP(A) at day 2
440 only; log2FC > 0.5 and adj. $p < 0.05$. (**F**) UMAP visualization as in (C), characterized by
441 labeling-based RNA velocity analysis. Streamlines indicate the integration paths that connect
442 local projections from the observed state to the extrapolated future state(*26*). (**G**) Pseudotemporal
443 ordering of top 200 DE genes and additional genes of interest ($q < 1.4 \times 10^{-17}$) between
444 trajectories. Gene labels correspond to all DE TFs in the T cell differentiation TF module (left
445 text) and DE target genes linked to *Tbx21*, *Egr1*, *Eomes*, and *Tcf7* (right text). (**H**) RNA velocity
446 and (**I**) Loess smoothed TF activity over pseudotime for four of the most DE genes between
447 trajectories. TF activity is calculated as the normalized aggregation of levels of newly
448 synthesized mRNA for all TF target genes, scaled across all cells. Cells in the undifferentiated
449 (U) cluster are set to pseudotime = 0 for each trajectory.
450
451

Figure 3

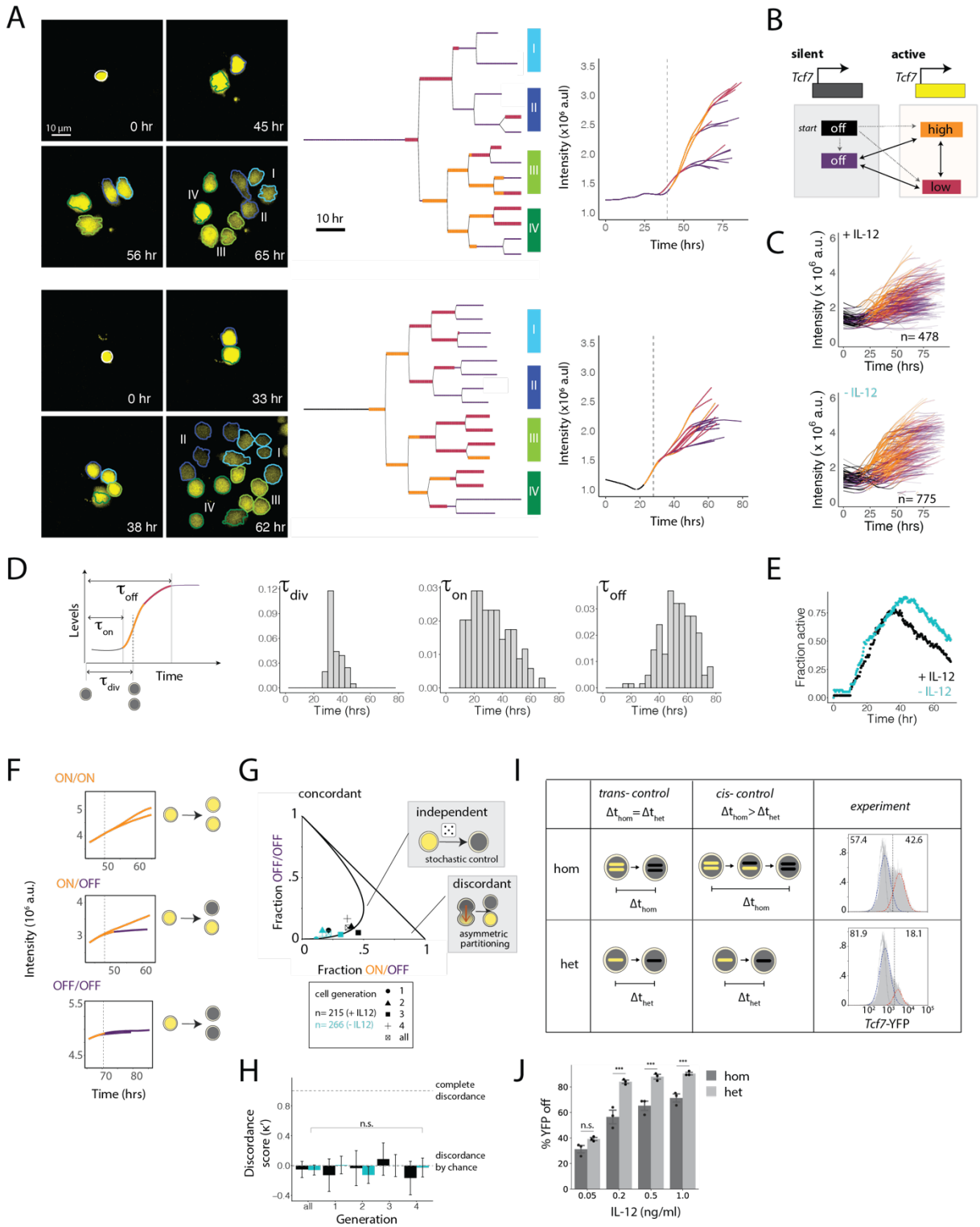
A
10 µm
0 hr
45 hr
56 hr
65 hr
10 hr
Intensity (x10⁶ a.u)
Time (hrs)
0 hr
33 hr
38 hr
62 hr
B
silent
active
Tcf7
start
off
high
low
C
+ IL-12
- IL-12
Intensity (x 10⁶ a.u.)
n= 478
n= 775
Time (hrs)
D
Levels
Time
τoff
τon
τdiv
Time (hrs)
E
Fraction active
+ IL-12
- IL-12
Time (hr)
F
ON/ON
ON/OFF
OFF/OFF
Intensity (10⁶ a.u.)
Time (hrs)
G
concordant
independent
stochastic control
discordant
asymmetric partitioning
Fraction OFF/OFF
Fraction ON/OFF
cell generation
n= 215 (+ IL12)
n= 266 (- IL12)
all
H
complete discordance
n.s.
discordance by chance
Discordance score (κ')
Generation
I
trans- control
cis- control
experiment
hom
het
57.4
42.6
81.9
18.1
Tcf7-YFP
J
hom
het
% YFP off
IL-12 (ng/ml)

452

453 **Figure 3: Heterogeneous *Tcf7* silencing within clones is controlled by a stochastic epigenetic**
454 **switch.** (**A**) Representative lineages demonstrating clonal heterogeneity in *Tcf7*-YFP silencing:
455 image snap shots (left), lineage trees (middle), and reporter intensity (area x median YFP levels)
456 over time for each track (right), with the first cell division marked by a vertical dashed line. Cell
457 borders in snapshots are colored and labeled to match their corresponding leaves in the lineage
458 trees. Lineage trees and tracks are colored by HMM-derived promoter state, outlined in (**B**).
459 Cells are cultured with 1 ng/ml IL-12 unless otherwise indicated. (**C**) Reporter intensity for all
460 overlaid tracks, colored by promoter state. (**D**) For each track, from left to right: time of first
461 division, time of first transition to a stable active state, time of first transition to a stable silent
462 state (stable state ≥ 10 hrs). (**E**) For all lineages combined, fraction of cells in an active promoter
463 state over time, +/- 1 ng/ml IL-12. (**F-H**) Each division of a parent cell with the *Tcf7* promoter
464 ON was categorized as giving rise to zero, one, or two daughters that transition to an OFF state.
465 (**F**) Examples of each division category. (**G**) The OFF/OFF fraction by ON/OFF fraction is
466 plotted separately for each generation, +/- IL-12, to distinguish concordant, independent, and
467 asymmetric silencing mechanisms. (**H**) Modified Cohen's kappa test for division events in (G).
468 (**I**) Comparison of YFP/YFP and YFP/+ reporters to distinguish *cis* and *trans* regulation of *Tcf7*
469 silencing (left). YFP distributions for YFP/YFP and YFP/+ reporters cultured for 5 days with 0.2
470 ng/ml IL-12 (right). YFP off fractions are calculated from gaussian fits to distributions. (**J**) YFP
471 off percentages as in (I), over a range of IL-12 concentrations. Mean ± s.d. Statistical
472 significance was calculated with an unpaired two-tailed t test; n.s. p=0.05, ***p<0.005.
473 Individual data points are from a single experiment representative of 2 independent experiments
474 (I-J).
475

Figure 4

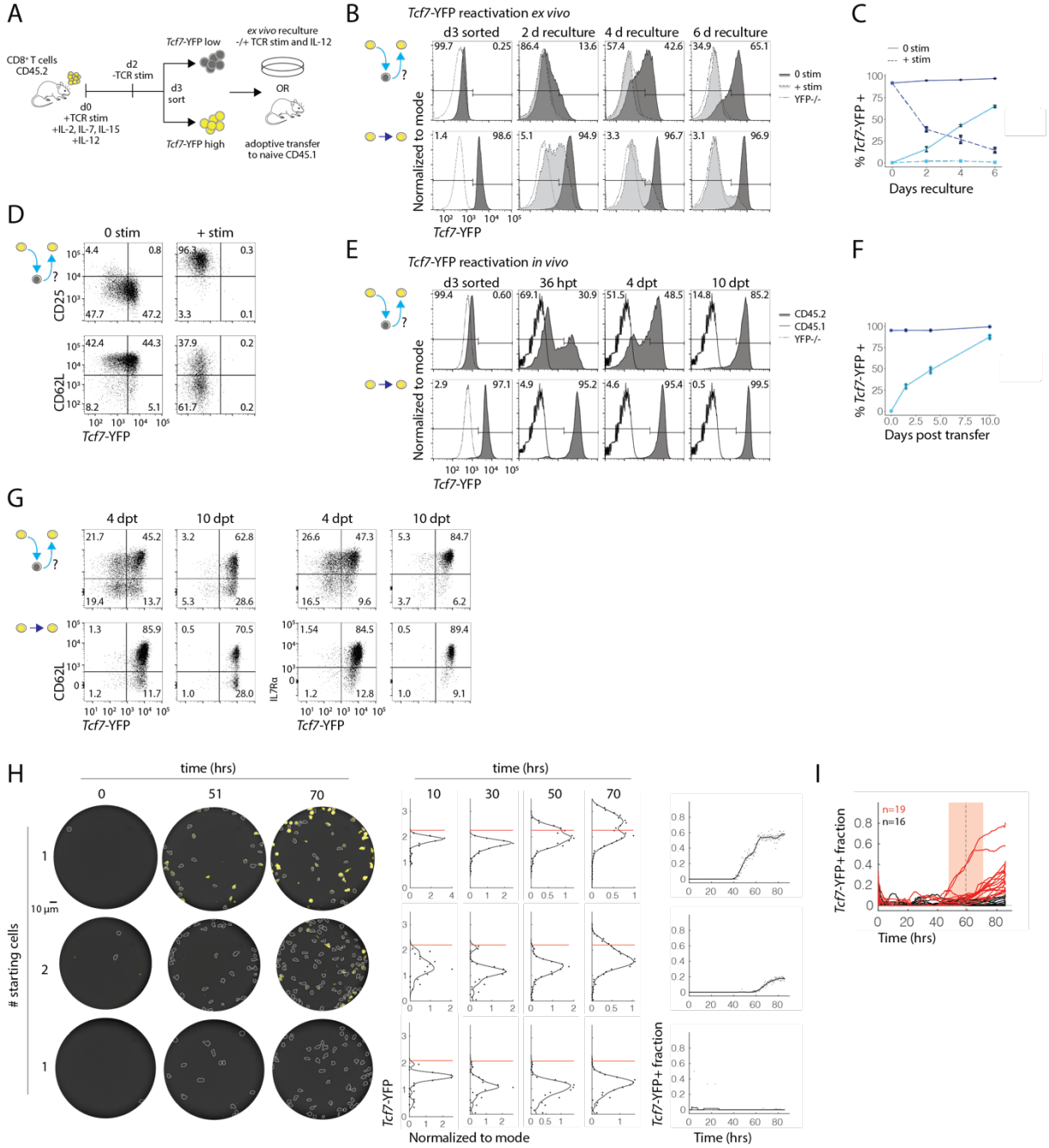

476

477 **Figure 4: Effector cells reverse *Tcf7* silencing and regain memory potential upon**

478 **stimulation withdrawal.** (**A**) Naive cells from *Tcf7*-YFP mice were stimulated as indicated,

479 sorted for *Tcf7*-YFP low and high populations after 3 days, and recultured either *ex vivo* (B-D,
480 H-I) or adoptively transferred to naive recipients (E-G). Light and dark blue coloring throughout
481 correspond to sorted YFP low and high populations, respectively. (**B-C**) *Tcf7*-YFP levels during
482 reculture with or without αCD3/αCD28 and IL-12 (+/- stim) compared to non-fluorescent
483 controls. **(D)** CD25, CD62L, and *Tcf7*-YFP expression in *Tcf7*-low sorted cells recultured +/-
484 stimulation. (**E-F**) *Tcf7*-YFP levels over time in $CD45.2^{+}CD45.1^{-}CD8^{+}$ cells harvested from the
485 spleen after sort and adoptive transfer to naive recipients. (**G**) CD62L and IL7Rα expression in
486 cells from E, F after *in vivo* transfer. (**H**) Representative microwells of sorted *Tcf7*-low cells
487 recultured without stimulation: snap shots (left), top and bottom wells represent single clones;
488 corresponding histograms (middle) with binned cell data for each time point, with YFP +/- gate
489 drawn at 2 standard deviations above the mean YFP intensity from the first 25 hrs;
490 corresponding YFP^{+} fractions over time (right). (**I**) YFP^{+} fraction for all wells overlaid. Mean
491 activation time = 59.1 hr. [C, F] Mean ± s.d. [B-D] Data are from a single experiment
492 representative of 1 and 3 independent experiments for +stim and 0 stim, respectively. [E-G] Data
493 are from a single experiment with n=3-4 biological replicates.
494

Figure 5

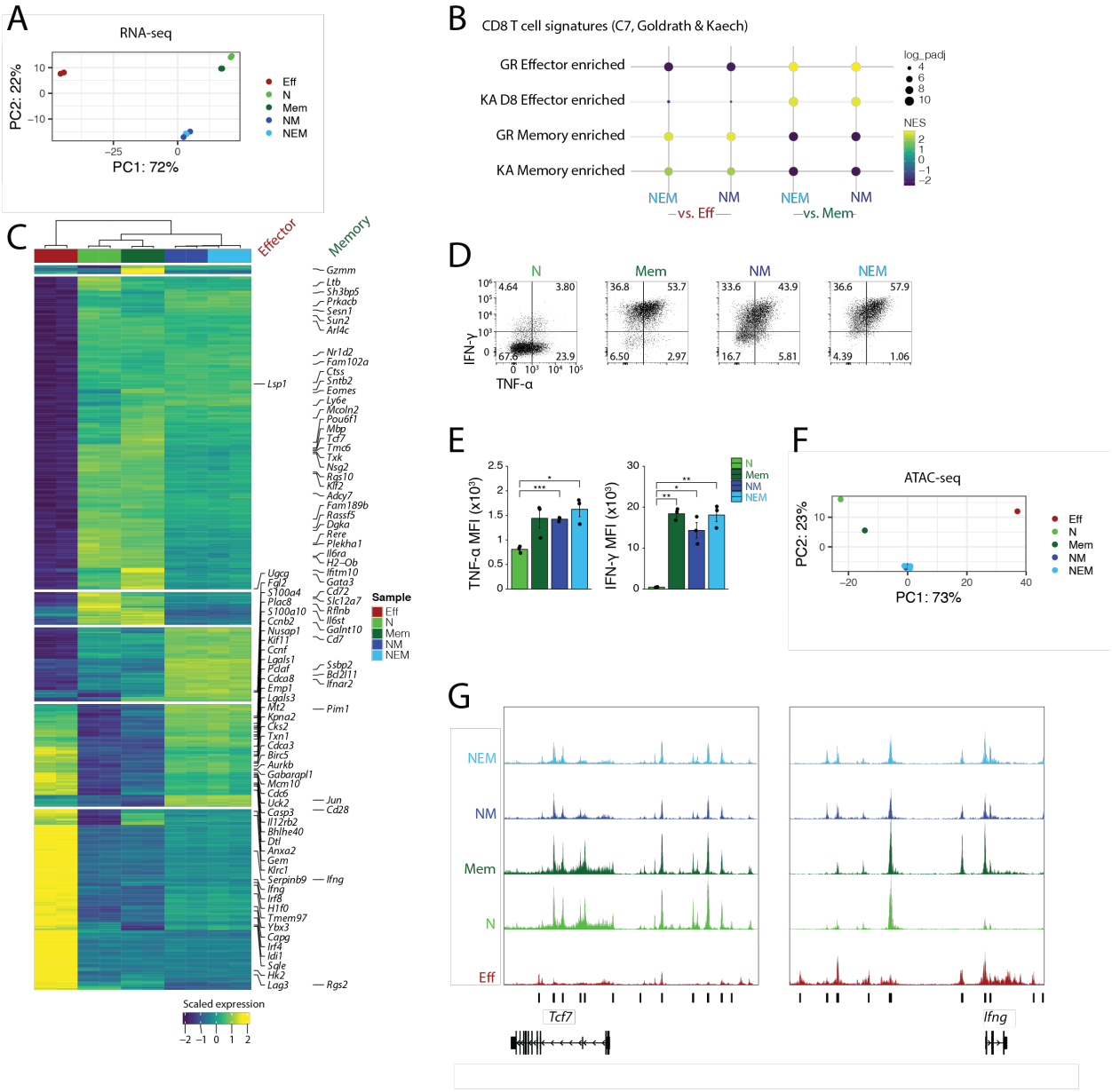

Figure 5: *Tcf7* high cells emerging from different routes acquire memory programming and functions. *Tcf7*-YFP low and high cells were sorted after 2 days of stimulation followed by one day of rest, recultured without TCR stimulation or IL-12 for an additional 6 days *ex vivo,* and then sorted for high *Tcf7*-YFP expression and subjected to genomic and functional analyses. (**A**) PCA of RNA-seq profiles (top 500 DE genes) for recultured cells compared to day 3 effector (Eff) and day 0 naive ($CD44^{-}CD62L^{+}$, N) and memory ($CD44^{+}CD62L^{+}$, Mem) controls. NM and

502 NEM cells were sorted as YFP-high and YFP-low on day 3, respectively. (**B**) GSEA of gene
503 signatures from MSigDB (C7, collections deposited by Goldrath (GR) and Kaech (KA)
504 comparing *ex vivo* recultured populations to Eff and Mem controls. (**C**) Heatmap displaying top
505 500 DE genes (lfc ≥ 2, Bonferroni-adjusted p value <0.05) between recultured populations and
506 Eff, N, and Mem controls. Scale bar indicates row z-scores of regularized log transformed count
507 data. Memory and effector associated genes from MSigDB Goldrath and Kaech collections are
508 highlighted. (**D-E**) Cytokine secretion of recultured cells compared to N and Mem controls after
509 PMA/Ionomcyin restimulation. (**F**) PCA of ATAC-seq counts of top 500 differentially accessible
510 peaks between recultured cells and controls. (**G**) ATAC-seq read coverage tracks; vertical bars
511 annotate differentially accessible peaks between recultured cells and controls. [A-C] n = 2
512 biological replicates for each sample. [D-E] Mean ± s.d. Statistical significance was calculated
513 with an unpaired two-tailed t test performed between groups. *p<0.5, **p<0.01, ***p<0.001.
514 Data are n=3 biological replicates from a single experiment. [F-G] n = 1 biological replicate for
515 Eff, N, Mem, n = 2 for NM, n = 3 for NEM.
516
517

Figure 6

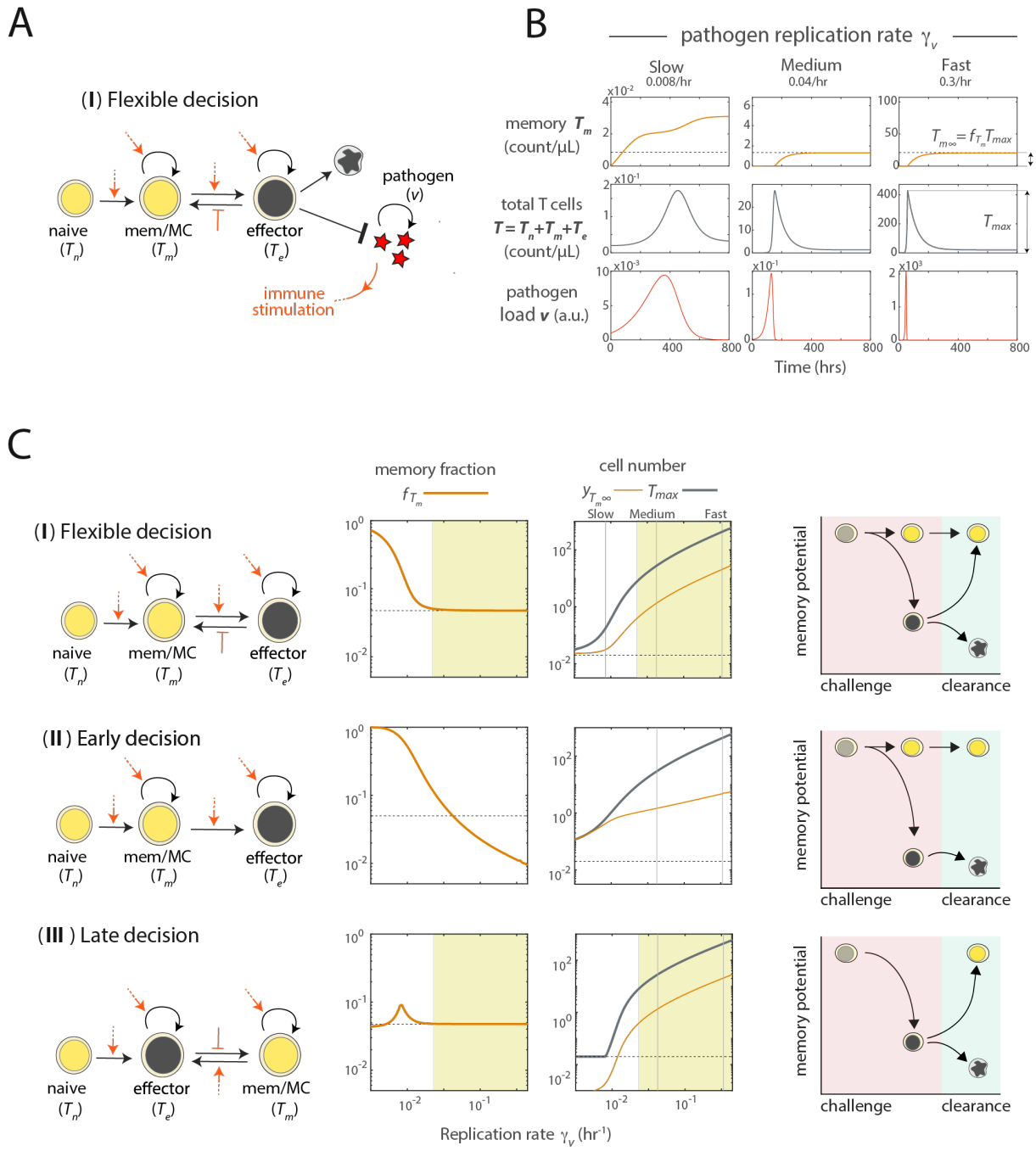

518

519 **Figure 6: Flexible decision making enables quantitative encoding of pathogen experience**

520 **during T cell memory formation.** (**A**) Model incorporates pathogen proliferation, T cell

521 memory decision making through reversible epigenetic switching. Orange arrows indicate

522 modulation of T cell state transitions by pathogen load. (**B**) Time traces show memory T cell

523 levels (top), total T cell levels (middle) and pathogen load (bottom), for different rates of
524 pathogen replication (left to right). Dotted line shows the number of memory T cells formed in
525 the case when this number is a defined fraction of the peak total T cell number, f_{Tm}. (**C**) Distinct
526 strategies for memory decision making: flexible (top), early (middle) or late (bottom); the
527 fraction of T cells at the response peak that become memory cells f_{Tm}; the peak cell number
528 (black) and memory cell number (orange), both plotted against pathogen replication rate γ_v. The
529 dotted line indicates the number of starting naive cells, and the yellow shading marks scalable
530 memory.
531

532 **Methods**

533

534 **Mice**

535 *Tcf7*-YFP mice have been described[16]. We note that a small number of experiments utilized mice
536 harboring an additional non-perturbing *Tbx21*-CFP BAC transgene reporter allele[46], though this
537 reporter was not further analyzed for this study. All mice used in experiments were heterozygous
538 for the *Tcf7*-YFP reporter except where specified. WT C57BL/6 mice (Jackson Laboratory) were
539 utilized as reporter negative controls, where applicable. Both male and female mice were used
540 for *ex vivo* experiments, aged 8 to 12 weeks. Female CD45.1 mice, 8-12 weeks of age, were
541 purchased from the Jackson Laboratory for use as recipients for adoptive transfer experiments.
542 For donors for adoptive transfer experiments, homozygous *Tcf7*-YFP mice were crossed with an
543 LCMV specific TCR transgenic strain[47] (P14) (Jackson Laboratory) and heterozygous offspring
544 were used. P14 homozygous mice without *Tcf7*-YFP were utilized as non-fluorescent controls

545 for sort gate setting. All mice were used in accordance with Institutional Animal Care and Use
546 Committee guidelines for the University of Washington.
547
548 **Naive T cell extraction**
549 Spleens were harvested from mice, massaged between rough glass slides to generate a single-cell
550 suspension, and filtered through 40 µm nylon mesh into HBH (HBSS, 10 mM HEPES, 0.5%
551 BSA, pH 7.4). Cells were spun down for 5 min at 300g, resuspended in 3 ml red blood cell
552 (RBC) lysis buffer (150 mM NH_4Cl, 10 mM $NaHCO_3$, 1 mM EDTA) for 3-5 min, and quenched
553 with HBH. Cells were spun down for 5 min at 300g and resuspended in HBH with 2.4G2
554 blocking solution and incubated for 30 min on ice. Cells were counted, spun down again, and
555 then enriched for CD8 T cells using a $CD8a^+$ T Cell Isolation Kit, mouse (Miltenyi, #130-104-
556 075), with the volume and amount of antibodies and microbeads used scaled down to 70% of
557 that specified by the manufacturer. One LS column was used per spleen (Miltenyi, # 130-042-
558 401). To obtain a pure population of naive CD8 T cells, the cell suspension was stained with
559 anti-CD8 (PerCP/Cyanine5.5, eBioscience, # 45-0081-82 or Biolegend, #100734), anti-CD44
560 (APC or PE, Invitrogen, #17-0441-82, or #12-0331-82), and anti-CD62L (APC/eFluor780,
561 Invitrogen, #47-0621-82) at 1:600 antibody to cell suspension volume ratio in $30x10^6$ cell/ml
562 HBH with Fc block for 15-30 min on ice and then sorted with a BD FACS Aria III (BD
563 Biosciences) with assistance from the University of Washington Pathology Flow Cytometry
564 Core Facility. The naive population was gated as $CD8^+CD44^-CD62L^+$*Tcf7*-YFP^+. Memory cells
565 were gated as $CD8^+CD44^+CD62L^+$*Tcf7*-YFP^+. The cells were sorted into HBH and kept on ice
566 until plating.
567

568 ***Ex vivo* T cell differentiation**

569 One day prior to T cell harvest and activation (day -1), plates were prepared by coating with anti-
570 CD3e (Tonbo, #40-0031-U100), anti-CD28 (Tonbo, #40-0281-U100), RetroNectin (Takara,
571 #T100B), and when specified, anti-CD11a (Biolegend, #101117). Unless otherwise specified,
572 each well of a 96-well plate received 0.2 µg anti-CD3, 0.1 µg anti-CD28, 1 µg Retronectin, and
573 (when specified) 1 µg anti-CD11a in 50 µL of PBS. For differentiation in larger wells, these
574 amounts were scaled up by well surface area. Plates were sealed with parafilm and incubated at
575 4°C overnight. On day 0, plates were allowed to come to room temperature for at least 30 min
576 and washed 2x with PBS. Purified cells were added to wells in T cell media [85% RPMI 1640
577 with L-glutamine, 10% Fetal Bovine Serum, Pen-Strep-Glutamine, 20 mM HEPES, 1 mM
578 Sodium Pyruvate, 0.1 mM NEAA, 50 µM BME] with indicated cytokine concentrations, mixed,
579 and spun down for 1 min at 150g to ensure initial contact for all cells with the coated plate
580 surface. Cytokines added to the media were 100 U/mL IL-2 (PeproTech, # 200-02), 0.5 ng/mL
581 IL-7 (PeproTech, # 200-07), 50 ng/mL IL-15 (PeproTech, # 210-15), and 1 ng/mL IL-12
582 (PeproTech, #210-12) unless otherwise specified. Where specified, IFN-β1 (Biolegend,
583 #581302) was added at 1000 U/mL. The cell seeding concentration was 0.1 - 2.5 million cells /
584 ml unless otherwise indicated. Cells were incubated at 37°C in 5% CO_2 and split every two days
585 by mixing, removing half of the well volume, and topping off the volume with TCM and
586 respective cytokines. Where applicable, prior to seeding, cells were stained with 5 µM CellTrace
587 Violet (CTV) (Invitrogen, #C34557) following the manufacturer's instructions.

588

589

590 **Flow cytometry analysis**

591 For timecourse analyses with cell surface protein staining, cells were spun down in round-bottom
592 96-well plates or 1.5 ml eppendorf tubes, resuspended in 2.4G2 blocking solution for 15-30 min
593 on ice, stained with cell surface antibodies at 1:1200 (anti-CD8: PerCP-Cyanine5.5, eBioscience,
594 # 45-0081-82, or Biolegend, #100734, anti-CD44: APC, Invitrogen, #17-0441-82, anti-CD62L:
595 APC-e780, Invitrogen #47-0621-82 , anti-CD25: APC, #17-0251-82), 1:400 (anti-CD45.1: APC,
596 Biolegend, #110714), 1:200 (anti-CD45.2: PE/Dazzle594, Biolegend, #109846) or 1:100 (anti-
597 CD127/IL7Rα: PE, Invitrogen, #12-1271-83) antibody to cell suspension volume ratio for an
598 additional 15-30 min on ice, and spun down again for a final resuspension in HBH prior to
599 acquisition. For samples that required intracellular protein staining, cells were fixed and
600 permeabilized using Cytofix/Cytoperm Fixation and Permeabilization kit (BD #554714)
601 according to manufacturer instructions and incubated with antibody for 30 min on ice. The TCF1
602 antibody (PE, BD Biosciences, #564271) and T-bet antibody (PE, Biolegend, #644809) were
603 used at 1:50 and 1:200, respectively. For samples that required intracellular cytokine staining,
604 cells were restimulated for 5 hr with PMA/Ionomycin (1x in 100 µL per sample Thermofisher,
605 #00-4970-93) in round-bottom 96-well plates, with a protein transport inhibitor (1x
606 Thermofisher, #00-4980-93) added after 1 hr. For cytokine secretion after sorting (for Naive,
607 Mem, and NM/NEM) cells were stained with Zombie Near IR at a 1:1000 dilution in PBS
608 following the manufacturer's instructions (Biolegend, #423117). Cells were then fixed,
609 permeabilized, and stained with antibodies for cytokine and other intracellular protein antibodies
610 as described above. All cytokine antibodies were used at 1:100 dilution in 1x BD Perm/Wash
611 buffer (anti-IFN-γ (APC/Cyanine7 or PE, Biolegend, #505849, #505808) and anti-TNF-α
612 (BV711 Biolegend, #506349). Data were acquired using an Attune Nxt Flow Cytometer
613 (ThermoFisher Scientific) and analyzed using FlowJo (BD) software.

614

615 **Sample processing for sci-fate-seq**

616 Naive CD8 T cells were activated *ex vivo*, as described. For this experiment, media was
617 supplemented with 100 U/mL IL-2, 0.5 ng/mL IL-7, 50 ng/mL IL-15, and 0.05 ng/mL IL-12.
618 The moderate level of IL-12, 0.05 ng/ml, was chosen for this experiment to produce a relatively
619 even representation of *Tcf7* high and low cells (see Fig. 1C). At days 1, 2, and 4 of activation,
620 two subsequent sci-fate time points were taken as follows: cells were mixed and split into two
621 wells, which had been coated with anti-CD3 and anti-CD28 at day -1 and remained in the
622 incubator with TCM; 4sU was added to one well for a final concentration of 200 μM, and that
623 well was harvested 2 hr later. At that time, 4sU was similarly added to the second well, and that
624 well was harvested 2 hr later. After each 4sU addition, cells were mixed and spun down at 150g
625 for 1 min. Harvested cells were prepared for sci-RNA-seq as described for the sci-fate protocol
626 [22]. Briefly, cells were fixed with ice-cold 4% PFA for 15 min, washed and flash frozen with
627 PBSR [PBS, pH 7.4, 0.2 mg/ml bovine serum albumin (Fisher), 1% SuperRnaseIn
628 (Thermofisher) and 10 mM dithiothreitol (DTT)]. PFA-fixed cells were thawed, washed, and
629 treated with iodoacetamide (IAA) to attach a carboxyamidomethyl group to 4sU. Following
630 these steps, a single-cell RNA sequencing library was prepared using the sci-RNA-seq
631 protocol[48,49]. The library was sequenced on the Illumina Next-seq system.

632

633 **Computational analysis for sci-fate-seq**

634

635 ***Read alignment, downstream processing, and TF module construction***

636 Read alignment and downstream processing, linking of TFs to regulated genes, and construction
637 of TF modules was performed as described in Cao et al., 2020, with minor modifications.
638 Briefly, for each gene, across all cells, the correlation between mRNA levels of each expressed
639 TF and that gene was computed using LASSO (least absolute shrinkage and selection operator)
640 regression. We sought to comprehensively define gene programs with distinct dynamics by
641 doing this correlation separately both using only newly synthesized transcript levels for potential
642 target genes and using overall transcript levels, expecting that target genes with more stable
643 transcripts would be more readily identified using newly synthesized transcripts, while less
644 abundant, more lowly detected target genes would be more readily identified in the overall
645 transcriptome. After filtering out the resultant covariance links with a correlation coefficient less
646 than 0.03, we identified 2,117 putative TF - target gene covariance links using newly synthesized
647 transcriptome levels and 9,927 using overall transcriptome levels, resulting in a total of 10,405
648 unique links after aggregation. These were further filtered to retain only links supported by ChiP-
649 seq binding, motif enrichment, or predicted enhancer binding[24], resulting in 1065 links between
650 51 TFs and 632 genes. Of these 1065 links, 147 were identified using the newly synthesized
651 transcriptome levels, 649 were identified using the overall transcriptome levels, and 269 were
652 identified by both. To calculate TF activity scores in each cell, newly synthesized unique
653 molecular identifier (UMI) counts for all linked target genes were scaled by library size, log
654 transformed, aggregated, and normalized. The absolute correlation coefficient was computed
655 between all TF pairs with respect to their activity across all cells. Pairwise correlations were
656 hierarchically clustered using the ward D2 method to identify TF modules, with the reasoning
657 that co-regulatory TFs must be simultaneously active within the same cell.
658

659 ***Cell ordering, clustering, and differential gene expression analysis between clusters***

660 We initially attempted to resolve T cell differentiation states by performing dimensionality
661 reduction with Uniform Manifold Approximation and Projection (UMAP) on whole or new
662 transcriptomes using all detected genes. This analysis largely separated cells by the time point at
663 which they were sampled (Fig. S2B), as previously observed[50,51], likely a consequence of the
664 host of other temporal changes occurring during activation apart from differentiation, such as cell
665 cycle control and metabolic programming. To characterize T cell differentiation dynamics apart
666 from other regulatory processes, cells were represented in UMAP space using newly synthesized
667 reads for all genes within the T cell differentiation TF module with monocle3 (v.0.2.3.0)
668 (reduction_method = 'UMAP', umap.n_neighbors = 15L, umap.min_dist = 0.001) [52] using the
669 function align_cds[53] to remove effects of cell cycle phase (preprocess_method = 'PCA',
670 alignment_group = 'Phase'). The resultant UMAP was clustered using density peak clustering[54],
671 which resulted in 5 main clusters (Fig. 2C, U and E2(A) combined, E1(A), E1(B), E2(B), and
672 MP(A) and MP(B) combined). To further resolve observed variable T cell differentiation marker
673 expression within two of these clusters, *k*-means clustering was used to further divide U and
674 E2(A) into separate states and MP(A) and MP(B) into separate states (k = 2 and 2.5,
675 respectively). Cells in different cell cycle phases were relatively evenly distributed across this
676 UMAP, with S phase representation highest in E1(A) (Fig. S2D). Differential gene expression
677 testing was performed between clusters using the monocle3 fit_models function.

678

679 ***RNA velocity analysis***

680 RNA velocity analysis and visualization of velocity streamlines was performed using Dynamo
681 (v.0.95.2.dev)[26] using expression matrices from the full and new transcriptome. The dataset was

682 subsetted to include only the T cell differentiation module genes prior to analysis, but the
683 resultant streamlines were similar when the analysis was performed with all genes. The
684 streamline results were also similar when scVelo (v.0.2.2)[55] was used for velocity analysis (data
685 not shown), with the full and new transcriptome used as the unspliced/spliced expression
686 matrices, indicating that the streamline results are consistent between multiple analysis methods.
687 The scVelo results were also similar with or without subsetting to include only the T cell
688 differentiation module genes.
689
690 ***Trajectory analysis***
691 Cells in each putative trajectory (E1, E2, MP) were ordered in pseudotime based on the point
692 position on the principal curve estimated using the princurve package[56]. To align the precursor
693 cells between trajectories, cells in the undifferentiated (U) cluster were set to pseudotime = 0. To
694 identify genes that distinguish the trajectories, differentially expressed genes were identified
695 using the monocle3 fit_models function with the model formula as the trajectory and pseudotime
696 terms. Only resulting DEG associated with the trajectory term were selected.
697
698 **Time-lapse imaging**
699 Long-term time-lapse imaging of cultured cells, both to track *Tcf7* regulation during initial
700 activation in naive cells and to track *Tcf7* reactivation in sorted *Tcf7*-low cells, was performed as
701 previously described with some modifications[57,58]. Images were acquired with an inverted
702 widefield fluorescence microscope (Leica DMi8) fit with an incubator to maintain a constant
703 humidified environment at 37°C and 5% CO2, using a 40X dry objective. For imaging of the
704 initial 4 days of activation (Fig. 3), cells were seeded at low density (2-5k c/well) in wells of a

705 96-well glass bottom plate (Mattek) coated with anti-CD3, anti-CD28, anti-CD11a, and
706 RetroNectin, as described above. For *Tcf7* reactivation imaging experiments (Fig. 4), *Tcf7*-low
707 cells were sorted on day 3 after 2 days of initial culture with anti-CD3 and anti-CD28 in media
708 with IL-2, IL-7, IL-15, and IL-12 and one additional day of culture with anti-CD3 and anti-CD28
709 removed. These cells were seeded onto PDMS micromesh (250 μm hole diameter,
710 Microsurfaces) mounted on top of a 24-well glass bottom plate (Mattek) to enable clonal
711 tracking, as seeded cells show considerably enhanced motility in the absence of TCR
712 stimulation. To prepare the micromesh for imaging, the surface was first coated with BSA while
713 mounted on top of a 24-well plate overnight at 4°C and then transferred to a new glass well and
714 coated with anti-CD11a and RetroNectin for improved adhesion but without anti-CD3 and anti-
715 CD28. For reactivation experiments, cells were cultured in TCM with IL-2, IL-7, and IL-15, but
716 without IL-12.
717
718 To determine if the experimental conditions required for imaging affect differentiation, we
719 systematically compared expression of CD44, CD62L, and *Tcf7*-YFP in cells activated on glass
720 or tissue culture plates, at high or low seeding density, and with or without presence of anti-
721 CD11a (Fig. S3L). CD44 levels were comparable across all conditions, confirming that all cells
722 activated in all conditions. In tissue culture plates, CD62L and *Tcf7*-YFP levels were also
723 comparable, though the *Tcf7*-YFP levels were slightly reduced at lower cell density, particularly
724 in the condition without IL-12, consistent with previous findings that memory differentiation
725 occurs less efficiently at lower cell densities[59]. On glass plates, the fraction of CD62L low cells
726 was increased compared to on tissue culture plates. *Tcf7* levels were similarly low for the
727 condition with IL-12, but the combination of low seeding density and presence of anti-CD11a on

728 the glass plate resulted in a lower *Tcf7* distribution in the no IL-12 condition than was otherwise
729 observed. This analysis shows that the specific conditions used for imaging do not affect overall
730 differentiation trends but may underestimate the differences in differentiation between conditions
731 with and without IL-12.
732
733 **Computational analysis for time-lapse imaging**
734
735 ***Image segmentation and tracking***
736 Image pre-processing, cell segmentation, and tracking was performed in MATLAB (Mathworks,
737 Natick, MA) using the ictrack movie analysis pipeline we described previously[58,60] (Fig. S3A-B),
738 modified to enable segmentation of cells from brightfield movies. Importantly, to segment cells
739 without additional fluorescent labels besides *Tcf7*-YFP, we first trained a convolutional neural
740 network (CNN) with a U-net architecture[61] to predict fluorescence images of whole cells from
741 brightfield images, using images of cell-trace violet labeled T cells as a training data set[27]. We
742 trained separate CNNs for the images acquired in 96-well plates (Fig. 3) and in microwells (Fig.
743 4), as predictions are optimal when images for training and prediction have similar features. For
744 each training dataset, hundreds of images of CTV-stained cells were acquired at multiple
745 timepoints during the process of interest (e.g. initial T cell activation or culture after stimulation
746 removal). Using the trained CNN, we then generated predicted whole-cell fluorescence images
747 from acquired brightfield movies, which were used for cell segmentation (Fig. S3B, 1.). Briefly,
748 in the ictrack analysis pipeline, images underwent (1) correction by subtraction of uneven
749 background signal stemming from the bottom of the glass plate or the side of the PDMS
750 microwells (2) Gaussian blur followed by pixel value saturation to fix uneven signal intensity

751 within the nucleus of the cell and (3) Laplacian edge detection algorithm to identify the nucleus
752 boundary. Non-cell objects were excluded via size and shape limit exclusions. To generate clonal
753 lineage trees, cells were tracked automatically between adjacent movie frames using the
754 Munkres assignment algorithm, and the resulting cell tracks were manually checked for errors
755 and to annotate cell divisions (Fig. S3B, 2.).
756
757 **Tcf7 *promoter state assignment and analysis***
758 To enable quantitative analysis of *Tcf7* promoter activity in clonal cell lineages, we assembled
759 separate full tracks of total *Tcf7*-YFP fluorescence levels from the starting cell to each ending
760 cell within a lineage tree, for all lineage trees analyzed (Fig. S3B, 3.). Fluorescence levels are
761 halved at each cell division; thus, to ensure continuity in *Tcf7*-YFP levels in these tracks, we
762 calculated for each parent-daughter cell pair an offset in *Tcf7*-YFP levels, that we added to the
763 daughter cells and their progeny, as previously implemented[32]. These 'continuized' tracks were
764 then smoothed using MATLAB medfilt1 (N=5) and smooth (span = 80 time points, equivalent to
765 20 hours, method = lowess), and their first derivatives with respect to time were calculated to
766 generate single-cell tracks of *Tcf7* promoter activity for downstream HMM analysis (Fig. S3B,
767 4.).
768
769 Cell tracks were exported from MATLAB to R for downstream processing. *Tcf7* promoter states
770 for each cell and time point were called from tracks of *Tcf7*-YFP level derivatives using Hidden
771 Markov Model (HMM) modeling, implemented with the msm Package for R (v1.6.9)[62]. We
772 initially tested four candidate HMM models with either three or four promoter states and variable
773 constraints on the derivative ranges within each state (Fig. S3C-D). For each model, we

774 constrained the mean and variance in *Tcf7* promoter activities of each state by fitting Gaussian
775 distributions to the *Tcf7*-YFP derivatives at different time windows, to reflect our observations
776 that cells are expected to be mostly in an inactive, active, or attenuated state at different times.
777 We then compared the performance of these four models by calculating their log-likelihood and
778 corresponding AIC (Akaike information criterion) scores. We also checked the quality of each
779 model's fit to the data by assessing whether residuals of the fit follow a Gaussian distribution[63]
780 (Fig. S3E). Based on this analysis, we chose a model in which cells transition between 4 states:
781 off (initial), low active, high active, and off (Fig. 3B, Fig. S3F), and all start in the off-initial
782 state at the beginning of the track. This four-state model performed favorably compared to other
783 models, likely because it better accounts for the distinct distributions of promoter activity of
784 silent and active cells at initial and later time points.
785
786 Using this four-state model, we assigned promoter activity states at each time point for each cell,
787 removing potentially spurious transient promoter states by finding all promoter states lasting less
788 than 8 hours and replacing them with the previously assigned promoter state. From these states,
789 we then identified promoter silencing events as those involving a switch from active (high or
790 low) to an inactive (off) state, and activation events as those involving a switch from inactive
791 (off-initial or off) to active (high or low) states. We did not allow transitions back to the starting
792 inactive (off-initial) state, as this state has a distinct *Tcf7* promoter activity distribution from the
793 later silent state (off), likely reflecting the distinct noise characteristics of *Tcf7*-YFP levels at
794 different stages after activation.
795

796 For analysis of *Tcf7* silencing between sister cells, we first assigned an ending cell state to all
797 cells in the dataset, representing the final promoter state of the cell prior to division or the end of
798 the cell track. Cells with a tracked duration of less than 3 hours and parents with ending cell state
799 durations of less than 10 hours were also excluded, to ensure the analysis only includes
800 sufficiently tracked cells and durable promoter states. We then collected all division events for
801 which the parent cell was in an ON promoter state prior to division and asked whether the
802 daughter cell tracks ended in an ON or OFF promoter state. We thus calculated the number of
803 division events that lead to no (ON/ON), unequal (ON/OFF), or concordant (OFF/OFF) daughter
804 silencing and then calculated the fractions of each category in the entire dataset and within each
805 generation. To statistically analyze the degree of discordance in *Tcf7* silencing decisions between
806 sister pairs by modifying Cohen's kappa statistical test for inter-rater reliability as follows:
807 division events were categorized as concordant (ON/ON or OFF/OFF) or discordant (ON/OFF)
808 between sisters. The modified Cohen's kappa coefficient, κ', was calculated as the observed
809 percentage of discordant events minus the percentage of discordant events expected by chance,
810 divided by 1 minus the percentage of discordant events expected by chance[64] (Supplementary
811 Table 4).
812
813 **Analysis of *Tcf7*-YFP negative fractions in homozygous and heterozygous reporter cells**
814 For analysis in Fig. 3I-J and Fig. S3K, YFP distributions were exported from FlowJo as csvs,
815 imported to Python, and represented as histograms. The positive and negative populations were
816 fit simultaneously as two gaussian distributions using the scipy.optimize.least_squares function
817 (scipy v1.5.2), and the gate between YFP positive and negative populations was identified as the
818 intersection between the gaussian curves. The silent fraction was then calculated as the sum of

819 the histogram below the gate divided by the sum of the entire histogram. Two-tailed unpaired t
820 tests between homozygous and heterozygous YFP silent fractions were performed using
821 scipy.stats.
822
823 **Sort and adoptive transfer or *ex vivo* reculture of activated cells**
824 Cells were cultured *ex vivo* in the presence of anti-CD3/28 (+TCR stim) and IL-2, IL-7, IL-12,
825 and IL-15 as described. On day 2, cells were transferred to a non-antibody-coated plate (-TCR
826 stim) but kept in the same cytokine environment until day 3 for sorting. For adoptive transfer
827 experiments only, CD8 T cells were activated directly after purifying with the Miltenyi CD8a$^+$ T
828 Cell Isolation Kit using 100% recommended reagent amounts, without further purifying naive
829 starting cells by sorting, and RetroNectin was not used during anti-CD3/anti-CD28 stimulation.
830 Prior to *ex vivo* activation, cells were stained with 2 or 5 μM CellTrace Violet (Invitrogen,
831 #C34557). For *ex vivo* reculture experiments, cells were sorted from a single CellTrace peak
832 representing cells that had undergone the same number of divisions over the 3 day culture period,
833 to ensure YFP differences were due entirely to *Tcf7* regulation differences and not cell division
834 differences. Cells were recultured with and without TCR stimulation and IL-12 (with IL-2, IL-7,
835 and IL-15 maintained except where specified), as labeled in each figure, for an additional 6-10
836 days. For genomics experiments, effector controls (Eff) were activated with TCR stimulation and
837 cytokines for 3 full days. For adoptive transfer, cells were sorted that had undergone at least 4
838 divisions. Cells were sorted on CellTrace Violet and *Tcf7*-YFP levels. The *Tcf7* low gate was set
839 using wild type non-fluorescent control cells that were stimulated identically *ex vivo.* Using this
840 negative gate, the top and bottom 20% of the YFP distribution were selected as *Tcf7* high and
841 low. Sorted cells were resuspended in PBS and transferred retro-orbitally (1 million cells

842 transferred per recipient) to naive CD45.1 mice. On days 1.5, 4, and 10 after adoptive transfer,
843 mice were euthanized, and blood, spleens, and lymph nodes were collected for flow cytometry.
844
845 **Blood and lymph node processing**
846 Blood was collected from euthanized mice by cardiac puncture. Red blood cells were lysed 2x
847 for 5 minutes at room temperature using 1x RBC lysis buffer (described in naive T cell
848 extraction), prior to proceeding with cell staining as described in Flow Cytometry Analysis.
849 Inguinal lymph nodes were harvested, and massaged over a 40 µm cell strainer and resuspended
850 for flow cytometry staining as described in Flow Cytometry Analysis.
851
852 **Sample processing for RNA-seq**
853 Cells were centrifuged at 500g for 5 minutes, resuspended in 350 µL of Trizol (Ambion), mixed
854 well, and frozen at -80°C for processing, starting from step 2 of the RNeasy micro kit (Qiagen,
855 #74004) following the manufacturer's instructions. After processing, RNA was resuspended in
856 RNase free water, quantified using a NanoDrop 2000c (Thermo Scientific), and shipped on dry
857 ice to Novogene Corporation Inc. (Sacramento, CA) for library preparation and sequencing.
858
859 **Computational analysis for RNA-seq**
860 Raw FASTQ files from RNA-seq paired-end sequencing were aligned to the GRCm38/mm10
861 reference genome using Kallisto (v0.46.1)[65], and the resultant transcript-level abundance
862 estimates were imported to genes by cells matrices using tximport (v1.18.0) for downstream
863 analysis. Transcripts with low counts (<10) were removed. Differentially expressed genes were
864 identified with DESeq2 (v1.30.1)[66]. PCA plots were generated using the top 500 differentially

865 expressed genes between NM and NEM samples and naive, memory, and effector controls.
866 Significantly differentially expressed genes were also used for gene set enrichment analysis,
867 performed with fgsea (v1.16.0)[67] and using gene sets from the C7 immunologic or the H
868 Hallmark gene-sets from Molecular Signatures Database deposited by Goldrath and Kaech.
869

870 **Sample processing for ATAC-seq**

871 After sorting, cells were centrifuged at 500g for 5 minutes then supernatant was aspirated
872 without disturbing the pellet. The pellets were resuspended in 100 µL of ATAC freezing buffer[68]
873 (50 mM Tris at pH 8.0, 25% glycerol, 5 mM $Mg(OAc)_2$, 0.1 mM EDTA, 5 mM DTT, 1× protease
874 inhibitor cocktail (Roche-noEDTA tablet), 1:2,500 superasin (Ambion)), flash frozen in liquid
875 nitrogen and stored at -80°C. On the day of processing, samples were thawed, centrifuged at 4°C
876 500g for 5 minutes, and washed with 100 µL of cold 1X PBS. Cells were again centrifuged and
877 resuspended in 100 µL Omni lysis buffer[69] (RSB with 0.1% NP40, 0.1% Tween 20 and 0.01%
878 Digitonin) and incubated on ice for 3 minutes, then quenched with 500 mL of RSB + 0.1%
879 Tween 20. Nuclei were pelleted at 500g for 5 minutes at 4°C, resuspended in 100 µL cold PBS
880 and counted. 50,000 nuclei were used per reaction, pelleted (500g for 5 min at 4°C), resuspended
881 in tagmentation master mix[69] (50 µL total: 25 µL 2X TD buffer, 16.5 µL 1x DPBS, 0.5 µL 1%
882 Digitonin, 0.5 µL 10% Tween 20, 5 µL water, 2.5 µL Tn5 enzyme), and incubated at 55°C for
883 30 minutes. Samples were purified using DNA Clean and Concentrate-5 (Zymo Research) and
884 eluted in EB buffer (10 mM Tris) for amplification of tagmented DNA. PCR amplifications were
885 performed using Illumina indexed primers and NEBNext High-Fidelity 2X PCR Master Mix.
886 SYBR green was added to each PCR reaction to monitor amplification before it reached
887 saturation. Samples in this study were amplified between 11-15 cycles using recommended

888 conditions[70]. Unpurified products were run on a 6% TBE gel for quality control. PCR
889 product/library were purified using DNA Clean and Concentrate-5 (Zymo Research) then ran on
890 a tapestation to visualize nucleosome distribution. The libraries were normalized to 2nM then
891 pooled equimolar for sequencing. Pooled libraries were loaded onto a NextSeq 500 High150
892 cycle kit at 1.5 pM loading concentration with paired ends sequencing (read 1: 74 cycles, read 2:
893 74 cycles, index 1: 10 cycles, index 2: 10 cycles).
894
895 **Computational analysis for ATAC-seq**
896 Raw ATAC-seq FASTQ files from paired-end sequencing were processed and aligned to the
897 mm10 mouse genome using the PEPATAC (v0.10.3)[71] pipeline, which uses bowtie2[72] for
898 alignment. Unmapped, unpaired, and mitochondrial reads were removed. Following alignment,
899 peak calling, merging across all samples, and annotation was performed using HOMER
900 (v4.10)[73]. Differentially accessible regions were identified using DESeq2. PCA plots were
901 generated using the top 500 differentially accessible regions between recultured samples and
902 naive, memory, and effector controls. Coverage tracks were generated from bigwig read
903 alignment files using karyoploteR (v1.14.1).
904
905 **Statistical Analysis**
906 All analyses and p or adjusted p value significance are listed with each figure caption. Statistics
907 were performed in R using the rstatix package (v0.7.0) or Python using scipy (v1.5.2).
908
909

910 **Supplementary tables**

911 **Table S1: Differential gene expression between all UMAP clusters in Fig. 2C.** These DEG
912 results are displayed in heatmap in Fig. 2D.

913 **Table S2: Differential gene expression results for pairwise comparisons between relevant**
914 **UMAP clusters in Fig. 2C.** These DEG results are displayed in volcano plots in Fig. 2E and Fig.
915 S2F.

916 **Table S3: Differential gene expression between E1, E2, and MP trajectories.** These DEG
917 results are displayed in Fig. 2G.

918 **Table S4: Discordance score calculation using modified Cohen's kappa coefficient.** Results
919 are displayed in Fig. 3H.

920 **Table S5: Analysis of *Tcf7*-YFP reactivation in microwells.** The number of microwells with a
921 given starting number of cells and the number of microwells with this number of starting clones
922 that gave rise to *Tcf7*-YFP reactivated cells is shown. Relevant to Fig. 4H-I.

923 **Table S6: Differentially expressed genes in each bulk RNA-seq cluster.** Relevant to Fig. 5C.

924

925 **Supplementary movies**

926 **Movie S1: *Tcf7*-YFP silencing within a clonal lineage.** Relevant to Fig. 3A.

927 **Movie S2: *Tcf7*-YFP reactivation example 1.** Relevant to Fig. 4H-I.

928 **Movie S3: *Tcf7*-YFP reactivation example 2.** Relevant to Fig. 4H-I.

929

930

931

932

933

934

935 **References**

936 1. Murali-Krishna, K., Altman, J.D., Suresh, M., Sourdive, D.J., Zajac, A.J., Miller, J.D.,
937 Slansky, J., and Ahmed, R. (1998). Counting antigen-specific CD8 T cells: a reevaluation of
938 bystander activation during viral infection. Immunity *8*, 177–187. 10.1016/s1074-
939 7613(00)80470-7.
940 2. Vijh, S., and Pamer, E.G. (1997). Immunodominant and subdominant CTL responses to
941 Listeria monocytogenes infection. J. Immunol. *158*, 3366–3371.
942 3. Busch, D.H., Pilip, I.M., Vijh, S., and Pamer, E.G. (1998). Coordinate Regulation of
943 Complex T Cell Populations Responding to Bacterial Infection. Immunity *8*, 353–362.
944 10.1016/S1074-7613(00)80540-3.
945 4. Kaech, S.M., Wherry, E.J., and Ahmed, R. (2002). Effector and memory T-cell
946 differentiation: implications for vaccine development. Nat. Rev. Immunol. *2*, 251–262.
947 10.1038/nri778.
948 5. Lin, W.-H.W., Nish, S.A., Yen, B., Chen, Y.-H., Adams, W.C., Kratchmarov, R., Rothman,
949 N.J., Bhandoola, A., Xue, H.-H., and Reiner, S.L. (2016). CD8 + T Lymphocyte Self-
950 Renewal during Effector Cell Determination. Cell Rep. *17*, 1773–1782.
951 10.1016/j.celrep.2016.10.032.
952 6. Chang, J.T., Palanivel, V.R., Kinjyo, I., Schambach, F., Intlekofer, A.M., Banerjee, A.,
953 Longworth, S.A., Vinup, K.E., Mrass, P., Oliaro, J., et al. (2007). Asymmetric T
954 Lymphocyte Division in the Initiation of Adaptive Immune Responses. Science *315*, 1687–
955 1691. 10.1126/science.1139393.
956 7. Kakaradov, B., Arsenio, J., Widjaja, C.E., He, Z., Aigner, S., Metz, P.J., Yu, B., Wehrens,
957 E.J., Lopez, J., Kim, S.H., et al. (2017). Early transcriptional and epigenetic regulation of
958 CD8+ T cell differentiation revealed by single-cell RNA sequencing. Nat. Immunol. *18*,
959 422–432. 10.1038/ni.3688.
960 8. Youngblood, B., Hale, J.S., Kissick, H.T., Ahn, E., Xu, X., Wieland, A., Araki, K., West,
961 E.E., Ghoneim, H.E., Fan, Y., et al. (2017). Effector CD8 T cells dedifferentiate into long-
962 lived memory cells. Nature *552*, 404–409. 10.1038/nature25144.
963 9. Bannard, O., Kraman, M., and Fearon, D.T. (2009). Secondary Replicative Function of
964 CD8+ T Cells That Had Developed an Effector Phenotype. Science *323*, 505–509.
965 10.1126/science.1166831.
966 10. Jacob, J., and Baltimore, D. (1999). Modelling T-cell memory by genetic marking of
967 memory T cells in vivo. Nature *399*, 593–597. 10.1038/21208.
968 11. Chung, H.K., McDonald, B., and Kaech, S.M. (2021). The architectural design of CD8+ T
969 cell responses in acute and chronic infection: Parallel structures with divergent fates. J. Exp.
970 Med. *218*, e20201730. 10.1084/jem.20201730.
971 12. Benjaafar, S., Morin, T.L., and Talavage, J.J. (1995). The strategic value of flexibility in
972 sequential decision making. Eur. J. Oper. Res. *82*, 438–457.
973 13. Tello-Ramos, M.C., Branch, C.L., Kozlovsky, D.Y., Pitera, A.M., and Pravosudov, V.V.
974 (2019). Spatial memory and cognitive flexibility trade-offs: to be or not to be flexible, that is
975 the question. Anim. Behav. *147*, 129–136.
976 14. Zhao, X., Shan, Q., and Xue, H.-H. (2021). TCF1 in T cell immunity: a broadened frontier.
977 Nat. Rev. Immunol. 10.1038/s41577-021-00563-6.
978 15. Jeannet, G., Boudousquie, C., Gardiol, N., Kang, J., Huelsken, J., and Held, W. (2010).
979 Essential role of the Wnt pathway effector Tcf-1 for the establishment of functional CD8 T

980 cell memory. Proc. Natl. Acad. Sci. *107*, 9777–9782. 10.1073/pnas.0914127107.
981 16. Harly, C., Kenney, D., Ren, G., Lai, B., Raabe, T., Yang, Q., Cam, M.C., Xue, H.-H., Zhao,
982 K., and Bhandoola, A. (2019). The transcription factor TCF-1 enforces commitment to the
983 innate lymphoid cell lineage. Nat. Immunol. *20*, 1150–1160. 10.1038/s41590-019-0445-7.
984 17. Mescher, M.F., Curtsinger, J.M., Agarwal, P., Casey, K.A., Gerner, M., Hammerbeck, C.D.,
985 Popescu, F., and Xiao, Z. (2006). Signals required for programming effector and memory
986 development by CD8+ T cells. Immunol. Rev. *211*, 81–92. 10.1111/j.0105-
987 2896.2006.00382.x.
988 18. Rubinstein, M.P., Lind, N.A., Purton, J.F., Filippou, P., Best, J.A., McGhee, P.A., Surh,
989 C.D., and Goldrath, A.W. (2008). IL-7 and IL-15 differentially regulate CD8+ T-cell subsets
990 during contraction of the immune response. Blood *112*, 3704–3712. 10.1182/blood-2008-06-
991 160945.
992 19. Xiao, Z., Casey, K.A., Jameson, S.C., Curtsinger, J.M., and Mescher, M.F. (2009).
993 Programming for CD8 T Cell Memory Development Requires IL-12 or Type I IFN. J.
994 Immunol. *182*, 2786–2794. 10.4049/jimmunol.0803484.
995 20. Danilo, M., Chennupati, V., Silva, J.G., Siegert, S., and Held, W. (2018). Suppression of
996 Tcf1 by Inflammatory Cytokines Facilitates Effector CD8 T Cell Differentiation. Cell Rep.
997 *22*, 2107–2117. 10.1016/j.celrep.2018.01.072.
998 21. Joshi, N.S., Cui, W., Chandele, A., Lee, H.K., Urso, D.R., Hagman, J., Gapin, L., and Kaech,
999 S.M. (2007). Inflammation Directs Memory Precursor and Short-Lived Effector CD8+ T
1000 Cell Fates via the Graded Expression of T-bet Transcription Factor. Immunity *27*, 281–295.
1001 10.1016/j.immuni.2007.07.010.
1002 22. Cao, J., Zhou, W., Steemers, F., Trapnell, C., and Shendure, J. (2020). Sci-fate characterizes
1003 the dynamics of gene expression in single cells. Nat. Biotechnol. *38*, 980–988.
1004 10.1038/s41587-020-0480-9.
1005 23. Erhard, F., Saliba, A.-E., Lusser, A., Toussaint, C., Hennig, T., Prusty, B.K., Kirschenbaum,
1006 D., Abadie, K., Miska, E.A., Friedel, C.C., et al. (2022). Time-resolved single-cell RNA-seq
1007 using metabolic RNA labelling. Nat. Rev. Methods Primer *2*, 1–18. 10.1038/s43586-022-
1008 00157-z.
1009 24. He, B., Xing, S., Chen, C., Gao, P., Teng, L., Shan, Q., Gullicksrud, J.A., Martin, M.D., Yu,
1010 S., Harty, J.T., et al. (2016). CD8 + T Cells Utilize Highly Dynamic Enhancer Repertoires
1011 and Regulatory Circuitry in Response to Infections. Immunity *45*, 1341–1354.
1012 10.1016/j.immuni.2016.11.009.
1013 25. Best, J.A., Blair, D.A., Knell, J., Yang, E., Mayya, V., Doedens, A., Dustin, M.L., and
1014 Goldrath, A.W. (2013). Transcriptional insights into the CD8+ T cell response to infection
1015 and memory T cell formation. Nat. Immunol. *14*, 404–412. 10.1038/ni.2536.
1016 26. Qiu, Q., Hu, P., Qiu, X., Govek, K.W., Cámara, P.G., and Wu, H. (2020). Massively parallel
1017 and time-resolved RNA sequencing in single cells with scNT-seq. Nat. Methods.
1018 10.1038/s41592-020-0935-4.
1019 27. Nguyen, P., Chien, S., Dai, J., Jr, R.J.M., Becker, P.S., and Kueh, H.Y. (2021). Unsupervised
1020 discovery of dynamic cell phenotypic states from transmitted light movies. PLOS Comput.
1021 Biol. *17*, e1009626. 10.1371/journal.pcbi.1009626.
1022 28. Verbist, K.C., Guy, C.S., Milasta, S., Liedmann, S., Kamiński, M.M., Wang, R., and Green,
1023 D.R. (2016). Metabolic maintenance of cell asymmetry following division in activated T
1024 lymphocytes. Nature *532*, 389–393. 10.1038/nature17442.
1025 29. Buchholz, V.R., Flossdorf, M., Hensel, I., Kretschmer, L., Weissbrich, B., Graf, P.,

1026 Verschoor, A., Schiemann, M., Hofer, T., and Busch, D.H. (2013). Disparate Individual
1027 Fates Compose Robust CD8+ T Cell Immunity. Science *340*, 630–635.
1028 10.1126/science.1235454.
1029 30. Duffy, K.R., Wellard, C.J., Markham, J.F., Zhou, J.H.S., Holmberg, R., Hawkins, E.D.,
1030 Hasbold, J., Dowling, M.R., and Hodgkin, P.D. (2012). Activation-Induced B Cell Fates Are
1031 Selected by Intracellular Stochastic Competition. Science *335*, 338–341.
1032 10.1126/science.1213230.
1033 31. Gerlach, C., Rohr, J.C., Perie, L., van Rooij, N., van Heijst, J.W.J., Velds, A., Urbanus, J.,
1034 Naik, S.H., Jacobs, H., Beltman, J.B., et al. (2013). Heterogeneous Differentiation Patterns
1035 of Individual CD8+ T Cells. Science *340*, 635–639. 10.1126/science.1235487.
1036 32. Bintu, L., Yong, J., Antebi, Y.E., McCue, K., Kazuki, Y., Uno, N., Oshimura, M., and
1037 Elowitz, M.B. (2016). Dynamics of epigenetic regulation at the single-cell level. Science
1038 *351*, 720–724. 10.1126/science.aab2956.
1039 33. Pease, N.A., Nguyen, P.H.B., Woodworth, M.A., Ng, K.K.H., Irwin, B., Vaughan, J.C., and
1040 Kueh, H.Y. (2021). Tunable, division-independent control of gene activation timing by a
1041 polycomb switch. Cell Rep. *34*, 108888. 10.1016/j.celrep.2021.108888.
1042 34. Lövkvist, C., Mikulski, P., Reeck, S., Hartley, M., Dean, C., and Howard, M. (2021). Hybrid
1043 protein assembly-histone modification mechanism for PRC2-based epigenetic switching and
1044 memory. eLife *10*, e66454. 10.7554/eLife.66454.
1045 35. Gray, S.M., Amezquita, R.A., Guan, T., Kleinstein, S.H., and Kaech, S.M. (2017). Polycomb
1046 Repressive Complex 2-Mediated Chromatin Repression Guides Effector CD8 + T Cell
1047 Terminal Differentiation and Loss of Multipotency. Immunity *46*, 596–608.
1048 10.1016/j.immuni.2017.03.012.
1049 36. Ladle, B.H., Li, K.-P., Phillips, M.J., Pucsek, A.B., Haile, A., Powell, J.D., Jaffee, E.M.,
1050 Hildeman, D.A., and Gamper, C.J. (2016). De novo DNA methylation by DNA
1051 methyltransferase 3a controls early effector $CD8^+$ T-cell fate decisions following activation.
1052 Proc. Natl. Acad. Sci. *113*, 10631–10636. 10.1073/pnas.1524490113.
1053 37. Pais Ferreira, D., Silva, J.G., Wyss, T., Fuertes Marraco, S.A., Scarpellino, L., Charmoy, M.,
1054 Maas, R., Siddiqui, I., Tang, L., Joyce, J.A., et al. (2020). Central memory CD8+ T cells
1055 derive from stem-like Tcf7hi effector cells in the absence of cytotoxic differentiation.
1056 Immunity *53*, 1–16. 10.1016/j.immuni.2020.09.005.
1057 38. Herndler-Brandstetter, D., Ishigame, H., Shinnakasu, R., Plajer, V., Stecher, C., Zhao, J.,
1058 Lietzenmayer, M., Kroehling, L., Takumi, A., Kometani, K., et al. (2018). KLRG1+ Effector
1059 CD8+ T Cells Lose KLRG1, Differentiate into All Memory T Cell Lineages, and Convey
1060 Enhanced Protective Immunity. Immunity *48*, 716–729. 10.1016/j.immuni.2018.03.015.
1061 39. Hou, S., Hyland, L., Ryan, K.W., Portner, A., and Doherty, P.C. (1994). Virus-specific
1062 CD8+ T-cell memory determined by clonal burst size. Nature *369*, 652–654.
1063 10.1038/369652a0.
1064 40. Plumlee, C.R., Sheridan, B.S., Cicek, B.B., and Lefrançois, L. (2013). Environmental Cues
1065 Dictate the Fate of Individual CD8+ T Cells Responding to Infection. Immunity *39*, 347–
1066 356. 10.1016/j.immuni.2013.07.014.
1067 41. Abadie, K., Pease, N.A., Wither, M.J., and Kueh, H.Y. (2019). Order by chance: origins and
1068 benefits of stochasticity in immune cell fate control. Curr. Opin. Syst. Biol. *18*, 95–103.
1069 10.1016/j.coisb.2019.10.013.
1070 42. Wagner, D.E., and Klein, A.M. (2020). Lineage tracing meets single-cell omics:
1071 opportunities and challenges. Nat. Rev. Genet. *21*, 410–427. 10.1038/s41576-020-0223-2.

1072 43. Weinreb, C., and Klein, A.M. (2020). Lineage reconstruction from clonal correlations. Proc.
1073 Natl. Acad. Sci. U. S. A. *117*, 17041–17048. 10.1073/pnas.2000238117.
1074 44. Xin, T., Gonzalez, D., Rompolas, P., and Greco, V. (2018). Flexible fate determination
1075 ensures robust differentiation in the hair follicle. Nat. Cell Biol. *20*, 1361–1369.
1076 10.1038/s41556-018-0232-y.
1077 45. Manz, M.G., and Boettcher, S. (2014). Emergency granulopoiesis. Nat. Rev. Immunol. *14*,
1078 302–314. 10.1038/nri3660.
1079 46. Zhu, J., Jankovic, D., Oler, A.J., Wei, G., Sharma, S., Hu, G., Guo, L., Yagi, R., Yamane, H.,
1080 Punkosdy, G., et al. (2012). The Transcription Factor T-bet Is Induced by Multiple Pathways
1081 and Prevents an Endogenous Th2 Cell Program during Th1 Cell Responses. Immunity *37*,
1082 660–673. 10.1016/j.immuni.2012.09.007.
1083 47. Pircher, H., Bürki, K., Lang, R., Hengartner, H., and Zinkernagel, R.M. (1989). Tolerance
1084 induction in double specific T-cell receptor transgenic mice varies with antigen. Nature *342*,
1085 559–561. 10.1038/342559a0.
1086 48. Cao, J., Packer, J.S., Ramani, V., Cusanovich, D.A., Huynh, C., Daza, R., Qiu, X., Lee, C.,
1087 Furlan, S.N., Steemers, F.J., et al. (2017). Comprehensive single-cell transcriptional profiling
1088 of a multicellular organism. Science *357*, 661–667. 10.1126/science.aam8940.
1089 49. Cao, J., Cusanovich, D.A., Ramani, V., Aghamirzaie, D., Pliner, H.A., Hill, A.J., Daza,
1090 R.M., McFaline-Figueroa, J.L., Packer, J.S., Christiansen, L., et al. (2018). Joint profiling of
1091 chromatin accessibility and gene expression in thousands of single cells. Science *361*, 1380–
1092 1385. 10.1126/science.aau0730.
1093 50. Arsenio, J., Kakaradov, B., Metz, P.J., Kim, S.H., Yeo, G.W., and Chang, J.T. (2014). Early
1094 specification of CD8+ T lymphocyte fates during adaptive immunity revealed by single-cell
1095 gene-expression analyses. Nat. Immunol. *15*, 365–372. 10.1038/ni.2842.
1096 51. Kurd, N.S., He, Z., Louis, T.L., Milner, J.J., Omilusik, K.D., Jin, W., Tsai, M.S., Widjaja,
1097 C.E., Kanbar, J.N., Olvera, J.G., et al. (2020). Early precursors and molecular determinants
1098 of tissue-resident memory $CD8^+$ T lymphocytes revealed by single-cell RNA sequencing.
1099 Sci. Immunol. *5*, eaaz6894. 10.1126/sciimmunol.aaz6894.
1100 52. Cao, J., Spielmann, M., Qiu, X., Huang, X., Ibrahim, D.M., Hill, A.J., Zhang, F., Mundlos,
1101 S., Christiansen, L., Steemers, F.J., et al. (2019). The single-cell transcriptional landscape of
1102 mammalian organogenesis. Nature *566*, 496–502. 10.1038/s41586-019-0969-x.
1103 53. Haghverdi, L., Lun, A.T.L., Morgan, M.D., and Marioni, J.C. (2018). Batch effects in single-
1104 cell RNA-sequencing data are corrected by matching mutual nearest neighbors. Nat.
1105 Biotechnol. *36*, 421–427. 10.1038/nbt.4091.
1106 54. Rodriguez, A., and Laio, A. (2014). Clustering by fast search and find of density peaks.
1107 Science *344*, 1492–1496. 10.1126/science.1242072.
1108 55. La Manno, G., Soldatov, R., Zeisel, A., Braun, E., Hochgerner, H., Petukhov, V.,
1109 Lidschreiber, K., Kastriti, M.E., Lönnerberg, P., Furlan, A., et al. (2018). RNA velocity of
1110 single cells. Nature *560*, 494–498. 10.1038/s41586-018-0414-6.
1111 56. Hastie, T., and Stuetzle, W. (1989). Principal Curves. J. Am. Stat. Assoc. *84*, 502–516.
1112 10.1080/01621459.1989.10478797.
1113 57. Kueh, H.Y., Champhekar, A., Nutt, S.L., Elowitz, M.B., and Rothenberg, E.V. (2013).
1114 Positive Feedback Between PU.1 and the Cell Cycle Controls Myeloid Differentiation.
1115 Science *341*, 670–673. 10.1126/science.1240831.
1116 58. Kueh, H.Y., Yui, M.A., Ng, K.K.H., Pease, S.S., Zhang, J.A., Damle, S.S., Freedman, G.,
1117 Siu, S., Bernstein, I.D., Elowitz, M.B., et al. (2016). Asynchronous combinatorial action of

1118 four regulatory factors activates Bcl11b for T cell commitment. Nat. Immunol. *17*, 956–965.
1119 10.1038/ni.3514.
1120 59. Polonsky, M., Rimer, J., Kern-Perets, A., Zaretsky, I., Miller, S., Bornstein, C., David, E.,
1121 Kopelman, N.M., Stelzer, G., Porat, Z., et al. (2018). Induction of CD4 T cell memory by
1122 local cellular collectivity. Science *360*, eaaj1853. 10.1126/science.aaj1853.
1123 60. Ng, K.K., Yui, M.A., Mehta, A., Siu, S., Irwin, B., Pease, S., Hirose, S., Elowitz, M.B.,
1124 Rothenberg, E.V., and Kueh, H.Y. (2018). A stochastic epigenetic switch controls the
1125 dynamics of T-cell lineage commitment. eLife *7*, e37851. 10.7554/eLife.37851.
1126 61. Ounkomol, C., Seshamani, S., Maleckar, M.M., Collman, F., and Johnson, G.R. (2018).
1127 Label-free prediction of three-dimensional fluorescence images from transmitted-light
1128 microscopy. Nat. Methods *15*, 917–920. 10.1038/s41592-018-0111-2.
1129 62. Jackson, C.H. (2011). Multi-State Models for Panel Data: The **msm** Package for *R*. J. Stat.
1130 Softw. *38*. 10.18637/jss.v038.i08.
1131 63. Lian, H., Thompson, W.A., Thurman, R., Stamatoyannopoulos, J.A., Noble, W.S., and
1132 Lawrence, C.E. (2008). Automated mapping of large-scale chromatin structure in ENCODE.
1133 Bioinformatics *24*, 1911–1916. 10.1093/bioinformatics/btn335.
1134 64. Cohen, J. (1960). A Coefficient of Agreement for Nominal Scales. Educ. Psychol. Meas. *20*,
1135 37–46. 10.1177/001316446002000104.
1136 65. Bray, N.L., Pimentel, H., Melsted, P., and Pachter, L. (2016). Near-optimal probabilistic
1137 RNA-seq quantification. Nat. Biotechnol. *34*, 525–527. 10.1038/nbt.3519.
1138 66. Love, M.I., Huber, W., and Anders, S. (2014). Moderated estimation of fold change and
1139 dispersion for RNA-seq data with DESeq2. Genome Biol. *15*, 550. 10.1186/s13059-014-
1140 0550-8.
1141 67. Korotkevich, G., Sukhov, V., Budin, N., Shpak, B., Artyomov, M.N., and Sergushichev, A.
1142 (2021). Fast gene set enrichment analysis. 060012. 10.1101/060012.
1143 68. Saunders, A., Core, L.J., Sutcliffe, C., Lis, J.T., and Ashe, H.L. (2013). Extensive
1144 polymerase pausing during Drosophila axis patterning enables high-level and pliable
1145 transcription. Genes Dev. *27*, 1146–1158. 10.1101/gad.215459.113.
1146 69. Corces, M.R., Trevino, A.E., Hamilton, E.G., Greenside, P.G., Sinnott-Armstrong, N.A.,
1147 Vesuna, S., Satpathy, A.T., Rubin, A.J., Montine, K.S., Wu, B., et al. (2017). An improved
1148 ATAC-seq protocol reduces background and enables interrogation of frozen tissues. Nat.
1149 Methods *14*, 959–962. 10.1038/nmeth.4396.
1150 70. Cusanovich, D.A., Hill, A.J., Aghamirzaie, D., Daza, R.M., Pliner, H.A., Berletch, J.B.,
1151 Filippova, G.N., Huang, X., Christiansen, L., DeWitt, W.S., et al. (2018). A Single-Cell
1152 Atlas of In Vivo Mammalian Chromatin Accessibility. Cell *174*, 1309-1324.e18.
1153 10.1016/j.cell.2018.06.052.
1154 71. Smith, J.P., Corces, M.R., Xu, J., Reuter, V.P., Chang, H.Y., and Sheffield, N.C. (2021).
1155 PEPATAC: an optimized pipeline for ATAC-seq data analysis with serial alignments. NAR
1156 Genomics Bioinforma. *3*, lqab101. 10.1093/nargab/lqab101.
1157 72. Langmead, B., and Salzberg, S.L. (2012). Fast gapped-read alignment with Bowtie 2. Nat.
1158 Methods *9*, 357–359. 10.1038/nmeth.1923.
1159 73. Heinz, S., Benner, C., Spann, N., Bertolino, E., Lin, Y.C., Laslo, P., Cheng, J.X., Murre, C.,
1160 Singh, H., and Glass, C.K. (2010). Simple Combinations of Lineage-Determining
1161 Transcription Factors Prime cis-Regulatory Elements Required for Macrophage and B Cell
1162 Identities. Mol. Cell *38*, 576–589. 10.1016/j.molcel.2010.05.004.